Tissue-specific enhancer-gene maps from multimodal single-cell data identify causal disease alleles

Saori Sakaue[1,2,3], Kathryn Weinand[1,2,3,4], Shakson Isaac[1,2,3,4], Kushal K. Dey[3,5], Karthik Jagadeesh[3,5], Masahiro Kanai[3,6,7,8], Gerald F. M. Watts[9], Zhu Zhu[9], Accelerating Medicines Partnership® RA/SLE Program and Network, Michael B. Brenner[9], Andrew McDavid[10], Laura T. Donlin[11,12], Kevin Wei[9], Alkes L. Price[3,5,13], Soumya Raychaudhuri[1,2,3,4,*]

1. Center for Data Sciences, Brigham and Women's Hospital, Harvard Medical School, Boston, MA, USA
2. Divisions of Genetics and Rheumatology, Department of Medicine, Brigham and Women's Hospital, Harvard Medical School, Boston, MA, USA
3. Program in Medical and Population Genetics, Broad Institute of MIT and Harvard, Cambridge, MA, USA
4. Department of Biomedical Informatics, Harvard Medical School, Boston, MA, USA
5. Department of Epidemiology, Harvard T. H. Chan School of Public Health, Boston, MA, USA
6. Analytic and Translational Genetics Unit, Massachusetts General Hospital, Boston, MA, USA
7. Stanley Center for Psychiatric Research, Broad Institute of MIT and Harvard, Cambridge, MA, USA
8. Center for Computational and Integrative Biology, Massachusetts General Hospital, Boston, MA, USA
9. Division of Rheumatology, Inflammation, and Immunity, Department of Medicine, Brigham and Women's Hospital and Harvard Medical School, Boston, MA, USA
10. Department of Biostatistics and Computational Biology, University of Rochester Medical Center, Rochester, NY, USA
11. Hospital for Special Surgery, New York, NY, USA
12. Weill Cornell Medicine, New York, NY, USA
13. Department of Biostatistics, Harvard T. H. Chan School of Public Health, Boston, MA, USA

*Address correspondence to:
Soumya Raychaudhuri
77 Avenue Louis Pasteur, Harvard New Research Building, Suite 250D
Boston, MA 02446, USA.
soumya@broadinstitute.org
617-525-4484 (tel); 617-525-4488 (fax)

Abstract

Translating genome-wide association study (GWAS) loci into causal variants and genes requires accurate cell-type-specific enhancer-gene maps from disease-relevant tissues. Building enhancer-gene maps is essential but challenging with current experimental methods in primary human tissues. We developed a new non-parametric statistical method, SCENT (Single-Cell ENhancer Target gene mapping) which models association between enhancer chromatin accessibility and gene expression in single-cell multimodal RNA-seq and ATAC-seq data. We applied SCENT to 9 multimodal datasets including > 120,000 single cells and created 23 cell-type-specific enhancer-gene maps. These maps were highly enriched for causal variants in eQTLs and GWAS for 1,143 diseases and traits. We identified likely causal genes for both common and rare diseases. In addition, we were able to link somatic mutation hotspots to target genes. We demonstrate that application of SCENT to multimodal data from disease-relevant human tissue enables the scalable construction of accurate cell-type-specific enhancer-gene maps, essential for defining non-coding variant function.

Main

Introduction

Genome-wide association studies (GWAS) have comprehensively mapped loci for human diseases[1–4]. These loci harbor untapped insights about causal mechanisms that can point to novel therapeutics[2,5]. However, only rarely are we able to define causal variants or their target genes. Of the hundreds of associated variants in a single locus, only one or a few may be causal; others are associated since they tag causal variants[2,6,7]. Moreover, causal genes are also challenging to determine, since causal variants lie in non-coding regions in 90% of the time[8–10], may regulate distant genes[11–13], and may employ context-specific regulatory mechanisms[14–17].

To define causal variants and genes, previous studies have used both statistical and experimental approaches. Statistical fine-mapping[18–23] can narrow the set of candidate causal variants, and is more effective when GWAS includes diverse ancestral backgrounds with different allele frequencies and linkage disequilibrium structures (LD)[24–28]. However, these approaches alone are seldom able to identify true causal variants with confidence[7,23,29–32]. To define causal genes, previous studies have built enhancer-gene maps, that can be used to prioritize causal variants in enhancers and link causal variants to genes they regulate. These maps often require large-scale epigenetic and transcriptomic atlases (e.g., Roadmap[33], BLUEPRINT[34], and ENCODE[35]). The enhancer-gene maps have been built from these atlases by correlating epigenetic activity (i.e., enhancer activity; e.g., histone mark ChIP-seq and bulk ATAC-seq) with gene expression (e.g., RNA-seq)[36,37], by combining epigenetic activity and probability of physical contact with the gene[38,39], or by integrating multiple linking strategies to create composite scores [40]. However, current methods largely use bulk tissues or cell lines. Bulk

data potentially (i) cannot be easily applied to rare cell populations (ii) obscures the cell-type-specific nature of gene regulation and (iii) requires hundreds of experimentally characterized samples, necessitating consortium-level efforts. While perturbation experiments (e.g., CRISPR interference[41] or base editing[42]) can point to causal links between enhancers and genes, they are difficult to scale because they require the cell- or tissue-type specific experimental protocols[43].

Advances in single-cell technologies offer new opportunities for building cell-type specific enhancer-gene maps. Multimodal protocols now enable joint capture of epigenetic activity by ATAC-seq alongside early transcriptional activity with nuclear RNA-seq[44–48] . These methods are easily applied at scale to cells in human primary tissues without disaggregation, enabling query of many samples from disease-relevant tissues. If we establish accurate links between open chromatin enhancers and genes in single cells, statistical power should exceed bulk-tissue-based methods since each observation is at a cell-level resolution. However, the sparse and non-parametric nature of RNA-seq and ATAC-seq in single-cell experiments makes confident identification of these links challenging. To date, most methods use linear regression models to link enhancers and genes (e.g., ArchR[49] and Signac[50]) despite these features or only utilize co-accessibility of regulatory regions from ATAC-seq but not gene expression from sc-RNA-seq (e.g., Cicero[51]). These previous methods have not generally demonstrated efficacy in practice for causal variant fine-mapping in complex traits.

In this context, we developed Single-Cell Enhancer Target gene mapping (SCENT), to accurately map enhancer-gene pairs where an enhancer's activity (i.e. peak accessibility) is

associated with gene expression across individual single cells. We use Poisson regression and non-parametric bootstrapping[52] to account for the sparsity and non-parametric distributions. We predicted that peaks with gene associations are more likely to be functionally important. We apply SCENT to 9 multimodal datasets to build 23 cell-type specific enhancer-gene maps. We show that SCENT enhancers are highly enriched in statistically fine-mapped likely causal variants for eQTL and GWAS. We use SCENT enhancer-gene map to define causal variants, genes, and cell types in common and rare disease loci and somatic mutation hotspots, which has not been previously demonstrated by conventional enhancer-gene mapping based on bulk-tissues.

Results

Overview of SCENT

To identify (1) active *cis*-regulatory regions and (2) their target genes (3) in a given cell type, we leveraged single-cell multimodal datasets. SCENT accurately identifies significant association between chromatin accessibility of regulatory regions (i.e., peaks) from ATAC-seq and gene expression from RNA-seq across individual single cells (**Figure 1a**). Those associations can be used for prioritizing (1) likely causal variants if they are in regulatory regions that are associated with gene expression, (2) likely causal genes if they are associated with the identified regulatory region and (3) the critical cell types based on which map the association is identified in. We assessed whether binarized chromatin accessibility in an ATAC peak is associated with gene expression counts in *cis* (< 500kb from gene body), testing one peak-gene pair at a time in each

115 cell type (see **Methods**). We tested each cell type separately to capture cell-type-specific gene
116 regulation and to avoid spurious peak-gene associations due to gene co-regulation across cell
117 types.

118 Since both RNA-seq and ATAC-seq data are generally sparse[50,53–56], we used Poisson
119 regression since it was a simple model that has been used effectively for sc-RNA-seq
120 analysis[54,57]:

121 $$E_i \sim Poisson(\lambda_i)$$

122 $$log(\lambda_i) = \beta_0 + \beta_{peak}X_{peak} + \beta_{\%mito}X_{\%mito} + \beta_{nUMI}X_{nUMI} + \beta_{batch}X_{batch}$$

123 where E_i is the observed expression count of ith gene, and λ_i is the expected count under
124 Poisson distribution. β_{peak} indicates the effect of chromatin accessibility of a peak on i th gene
125 expression (see **Methods**) and reflects the strength of the regulatory effect and sign (i.e.,
126 enhancing vs. silencing effect). We accounted for donor or batch effects (X_{batch}) and cell-level
127 technical factors such as percentage of mitochondrial reads ($X_{\%mito}$).

128 However, gene expression counts are highly variable across genes (**Figure 1b**;
129 **Supplementary Figure 1a**), and Poisson regression might be suboptimal for highly expressed
130 and dispersed genes. Consequently, we observed inflated statistics when we permuted cell
131 barcodes to disrupt association between ATAC and RNA profiles (**Supplementary Figure 1b**).
132 Common analytical statistical models (e.g., linear, negative binomial and Poisson regression) all
133 demonstrated inflated statistics (**Supplementary Figure 1c-e**). Therefore, to accurately
134 estimate the error and significance of β_{peak}, we implemented non-parametric bootstrapping
135 framework. Briefly, we resampled cells with replacement from the full data and re-estimated

β'_{peak} up to 50,000 times. We compared this empirical distribution of β'_{peak} against null hypothesis (β'_{peak} = 0) to derive the significance of β_{peak} (i.e., two-sided bootstrapping-based *P* value; see **Methods, Supplementary Figure 2**). The Poisson regression followed by bootstrapping resulted in well-calibrated statistics with appropriate type I error (**Supplementary Figure 1f**).

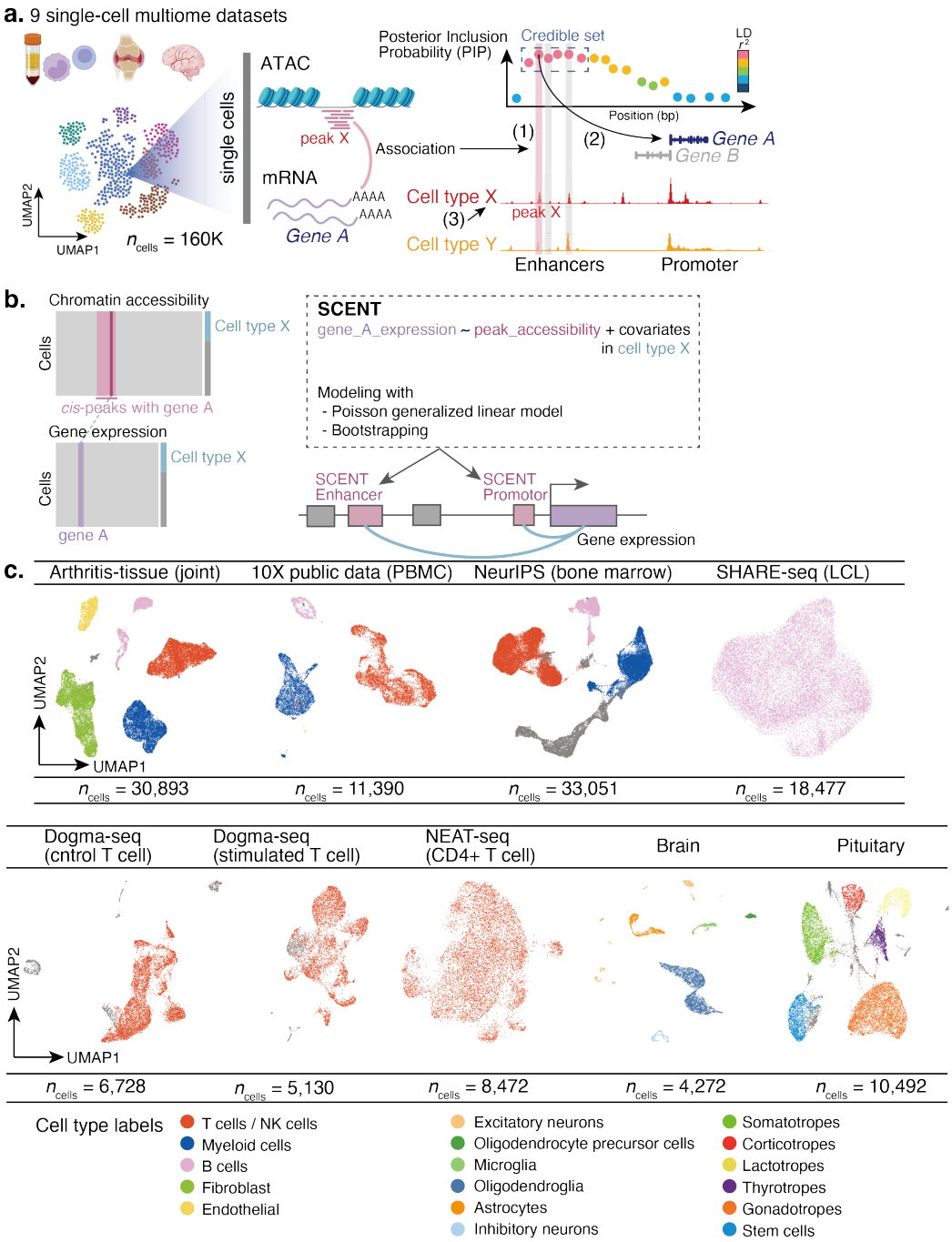

Figure 1. Schematic overview of SCENT and SCENT enhancer-gene pairs across 9 single-cell multimodal datasets. a. SCENT identifies (1) active *cis*-regulatory regions and (2) their target genes in (3) a specific cell type. Those SCENT results can be used to define likely causal variants, genes, and cell types for GWAS loci. **b**. SCENT models association between chromatin accessibility from ATAC-seq and gene expression from RNA-seq across individual cells in a given cell type. **c**. 9 single-cell datasets on which we applied SCENT to create 23 cell-type-specific enhancer-gene map. The cells in each dataset are described in UMAP embeddings from RNA-seq and colored by cell types.

150 *Discovery of cell-type-specific SCENT enhancer-gene links*

151 We obtained nine single-cell multimodal datasets from diverse human tissues representing 13
152 cell-types (immune-related, hematopoietic, neuronal, and pituitary). Since we are interested in
153 autoimmune diseases, we newly generated an inflammatory tissue dataset by obtaining inflamed
154 synovial tissues from ten rheumatoid arthritis (RA) and two osteoarthritis (OA) patients (arthritis-
155 tissue dataset; n_{donor} = 12). Applying stringent QC to these multimodal data, we obtained
156 information on 30,893 cells (see **Methods**). In addition, we obtained eight public datasets with
157 129,672 cells. In total we had data from 160,565 cells[46,58–62]. We analyzed 16,621 genes and
158 1,193,842 open chromatin peaks in *cis* after QC (4,753,521 peak-gene pairs, 28 median peaks
159 per gene; **Figure 1c**, **Supplementary Figure 3**, **Supplementary Table 1**). After clustering cells
160 and cell type annotation, we applied SCENT individually to each of the cell types with n_{cells} > 500
161 to construct 23 enhancer-gene maps. SCENT identified 87,648 cell-type-specific peak-gene
162 links (false discovery rate (FDR) < 10%, **Figure 2a**, **Supplementary Figure 4**). Each gene had
163 variable number of associated peaks in *cis* (from 0 to 97, mean = 4.13, **Supplementary Figure**
164 **5a**).

165 To assess replicability of SCENT peak-gene links, we compared the effects from the
166 arthritis-tissue dataset (discovery; which had the largest number of significant peak-gene pairs)
167 with those from other datasets in the same cell-type (replication) in B cells, T/NK cells and
168 myeloid cells (**Supplementary Table 2a**). Despite different tissue contexts, we confirmed high
169 directional concordance of the effect of chromatin accessibility on gene expression for peak-
170 gene pairs significant in both datasets (mean Pearson r = 0.62 of effect sizes, 99% mean

171 concordance across all the datasets: **Supplementary Figure 5b**). For comparison, we tested
172 two popular linear parametric single-cell multimodal methods that are already published, namely
173 ArchR[56] or Signac[50]. Using arthritis-tissue dataset as a discovery and public PBMC as a
174 replication, we noted lower directional concordance and effect correlation in these methods than
175 in SCENT (mean Pearson's r = 0.31, 62% mean directional concordance in ArchR and r = 0.24,
176 98% mean directional concordance in Signac; **Supplementary Table 2b** and **c**). These results
177 argue that SCENT can more reproducibly detect enhancer-gene links compared with previous
178 parametric methods for single-cell multimodal data.
179

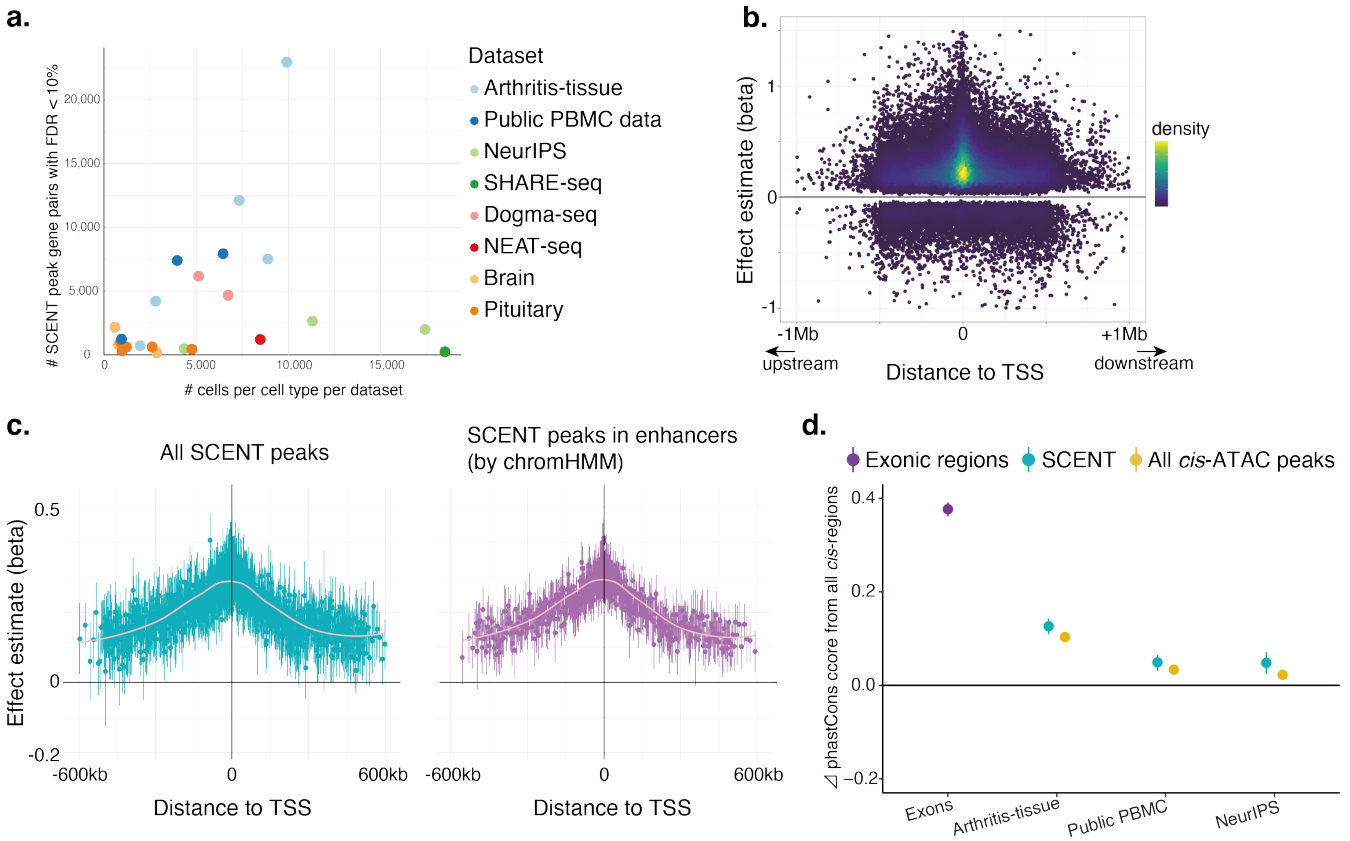

Figure 2. SCENT identified functionally active and evolutionary conserved *cis*-regulatory regions from single-cell multimodal data.
a. The number of significant gene-peak pairs discovered by SCENT with FDR < 10%. Each dot represents the number of significant gene-peak pairs in a given cell type in a dataset (y-axis) as a function of the number of cells in each cell type in a dataset (x-axis), colored by the dataset. **b**. The effect size (beta) of chromatin accessibility on the gene expression from Poisson regression (y-axis). Each dot is a significant gene-peak pair and plotted against the distance between the peak and the transcription start site (TSS) of the gene, colored as a density plot. **c.** The mean effect size (beta) of chromatin accessibility on the gene expression in arthritis-tissue dataset within each bin of TSS distance. Left; all significant gene-peak links. Right; SCENT peaks within enhancers identified using chromHMM in immune-related tissues. **d**. Mean phastCons score difference (Δ phastCons score) between each annotated region and all *cis*-regulatory non-coding regions. We show the Δ phastCons score for exonic regions (purple) as a reference, and for SCENT (green) and all *cis*-ATAC peaks (yellow) enhancers in each multimodal dataset.

To assess if SCENT peaks (i.e., *cis*-regulatory regions) were functional, we examined if (1) they co-localized with conventional *cis*-regulatory annotation, (2) their effect on expression was greater for closer peak-gene pairs, (3) they had high sequence conservation, and (4) peak-gene connections were more likely to be validated experimentally.

First, we tested the overlap of SCENT peaks with an ENCODE cCRE[63], a conventional *cis*-regulatory annotation by bulk epigenomic datasets. We observed that 98.0% of the SCENT peaks overlapped with ENCODE cCRE on average, compared to 23.3% of random *cis*-regions matched for size and 89.0% of non-SCENT peaks (**Supplementary Figure 5c**).

Second, we examined the strength of enhance-gene links, hypothesizing that stronger links would be more proximal to the transcription start site (TSS) of target genes. The regression coefficient β_{peak} (the effect size of peak accessibility on gene expression) became larger and more positive as the SCENT peaks got closer to the TSS (**Figure 2b** and **Figure 2c,** left panel), consistent with previous observations[56,64]. We annotated SCENT peaks with 18-state chromHMM results from 41 immune-related samples in ENCODE consortium[37]. When we subset peaks to those within enhancer annotations, we observed a clearer decay in β_{peak} as a function of TSS distance (**Figure 2c,** right panel).

Third, we assessed whether SCENT peaks had higher sequence conversation across species, quantified as phastCons score[66], which should indicate functional importance; the evolutionary conserved regulatory regions are known to be enriched for complex trait heritability[65]. As expected, exonic regions were much more evolutionary conserved than all non-coding *cis*-region (mean Δ phastCons score = 0.38, paired t-test $P < 10^{-323}$; **Figure 2d**, purple).

217 The SCENT regulatory regions were also conserved relative to non-coding *cis*-regions (mean Δ
218 phastCons score = 0.13, paired t-test $P = 4.2 \times 10^{-42}$ in arthritis-tissue dataset; **Figure 2d**, green).
219 In contrast, the Δ phastCons score between all *cis*-ATAC peaks and all non-coding *cis*-region
220 was more modest (mean Δ phastCons score = 0.092, paired t-test $P = 8.7 \times 10^{-27}$ in arthritis-
221 tissue dataset; **Figure 2d**, yellow). To test if the higher conservation in SCENT peaks were
222 driven by their proximity to TSS (**Supplementary Figure 6a**), we matched each of the SCENT
223 peak-gene pairs to one non-SCENT peak-gene pair that had the most similar TSS distance
224 (**Supplementary Figure 6b**). We assessed Δ phastCons score between SCENT peaks and
225 non-SCENT peaks with matching peaks on TSS distance. SCENT peaks had significantly higher
226 conservation scores than the non-SCENT peaks with the matched TSS distance (mean Δ
227 phastCons score = 0.034, $P = 4.7 \times 10^{-4}$ in arthritis-tissue dataset; **Supplementary Figure 5d**;
228 see **Methods**). The higher sequence conservation suggested the functional importance of
229 SCENT regulatory regions not solely driven by TSS proximity.

230 Finally, we tested whether the target genes from SCENT were enriched for experimentally
231 confirmed enhancer-gene links. We used Nasser et al.[39] CRISPR-Flow FISH results which
232 included 278 positive enhancer-gene connections and 5,470 negative connections. The SCENT
233 peaks were >4-fold enriched relative to non-SCENT peaks for positive connections (Fisher's
234 exact OR=4.5X, $P=1.8 \times 10^{-9}$ in arthritis-tissue dataset and 4.5X, $P=1.0 \times 10^{-8}$ in public PBMC
235 dataset; **Methods, Supplementary Table 3**).

236 We anticipate that the genes with the largest number of SCENT peaks are likely to be the
237 most constraint and least tolerant to loss of function mutations. The genes with the most SCENT

238 peaks included *FOSB* (*n* = 97), *JUNB* (*n* = 95), and *RUNX1* (*n* = 77), critical and highly conserved
239 transcription factors. We used mutational constraint metrics based on the absence of deleterious
240 variants within human populations (i.e., the probability of being loss-of-function intolerant (pLI)[67]
241 and the loss-of-function observed/expected upper bound fraction (LOEUF)[68]). The normalized
242 number of SCENT peaks per gene is strongly associated with mean constraint score for the
243 gene (beta=0.37, P=4.9x10^{-90} for pLI where higher score indicates more constraint, and beta=-
244 0.35, P=-0.35x10^{-106} for LOEUF where lower score indicates more constraint; **Supplementary**
245 **Figure 7a** and **7b**, respectively). Previously, genes with many regulatory regions from bulk-
246 epigenomic data had been shown to be enriched for loss-of-function intolerant genes[69]. We
247 replicated the same trend in the single-cell multimodal datasets and SCENT.
248
249 *Enrichment of eQTL putative causal variants in SCENT peaks*
250 We examined whether the SCENT peaks are likely to harbor statistically fine-mapped putative
251 causal variants for expression quantitative loci (eQTL). We used tissue-specific eQTL fine-
252 mapping results from GTEx across 49 tissues[70] and defined any variants with posterior inclusion
253 probability (PIP) > 0.2 as putative causal variants. We computed enrichment statistics within
254 ATAC peaks or SCENT peaks (see **Methods**). Unsurprisingly, all the accessible regions defined
255 by ATAC-seq in *cis*-regions were modestly enriched in fine-mapped variants by 2.7X (yellow,
256 **Figure 3a**). However, SCENT peaks were more strikingly enriched in fine-mapped variants by
257 9.6X on average across all datasets (green, **Figure 3a**). Using more stringent PIP threshold

258 cutoffs (0.5 and 0.7) to define putative causal variants resulted in even stronger enrichments
259 (**Supplementary Figure 8**).

260 Since many SCENT peaks are close to TSS regions, we again considered whether this
261 enrichment might be driven by TSS proximity (**Supplementary Figure 6a**). To test this, we
262 compared the fine-mapped variant enrichment between SCENT and non-SCENT peak-gene
263 pairs with matched TSS distance (**Supplementary Figure 6b**). The SCENT peaks consistently
264 had higher enrichment in all analyzed datasets (**Supplementary Figure 9a**) than TSS-
265 distance-matched non-SCENT peaks (e.g., 12.3X in SCENT vs. 9.64X in distance-matched
266 non-SCENT in arthritis-tissue dataset). This suggests that SCENT has additional information in
267 identifying functional *cis*-regulatory regions beyond TSS distance.

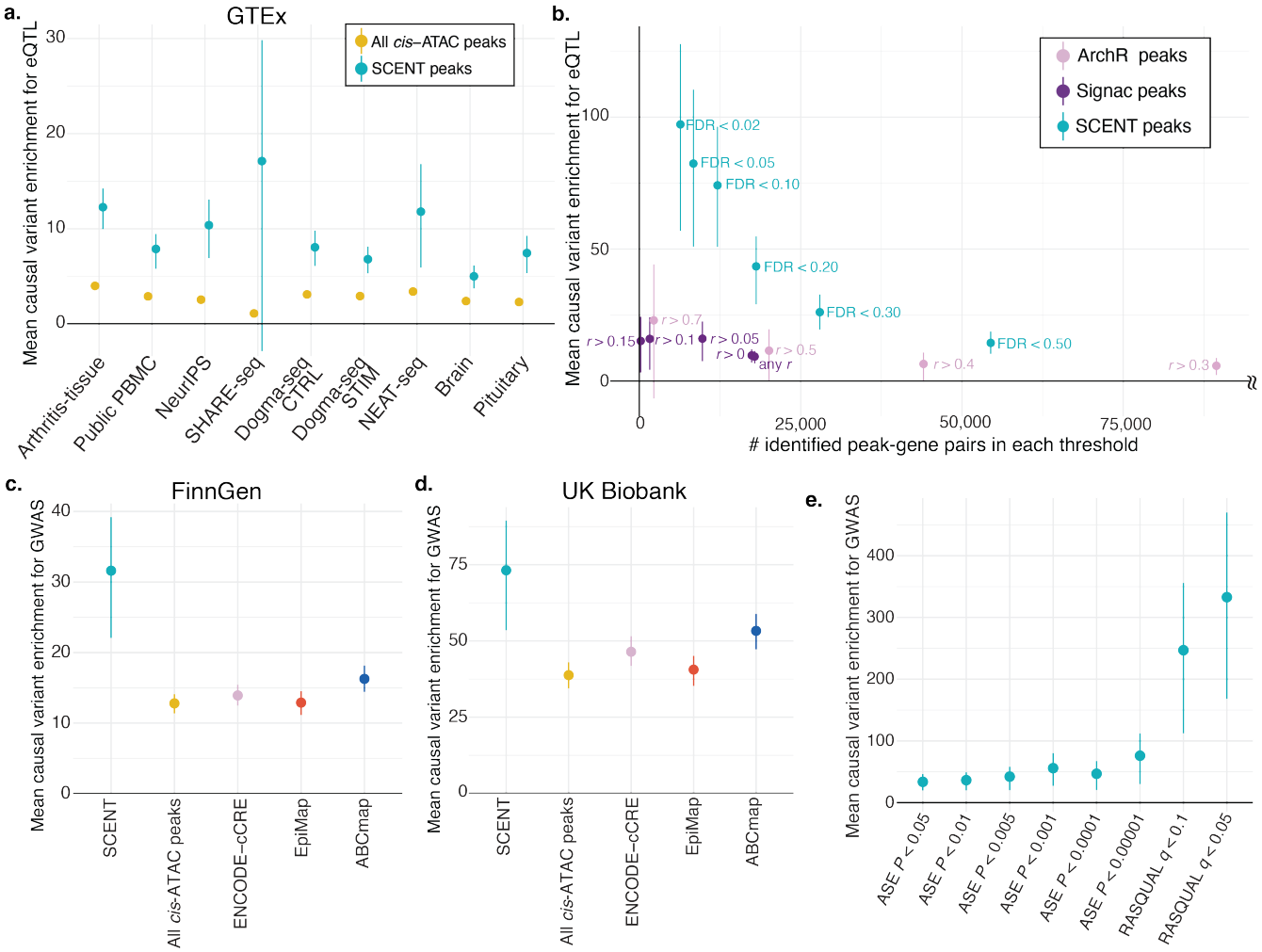

Figure 3. SCENT enhancers are enriched in putative causal variants of eQTL and GWAS. **a**. The mean causal variant enrichment for eQTL within SCENT peaks or all ATAC-seq peaks in each of the 9 single-cell datasets. The bars indicate 95% confidence intervals by bootstrapping genes. **b**. Comparison of the mean causal variant enrichment for eQTL (y-axis) between SCENT (green), ArchR (pink), and Signac (purple) as a function of the number of significant peak-gene pairs at each threshold of significance. The bars indicate 95% confidence intervals by bootstrapping genes. The ArchR results with > 100,000 peak-gene linkages are omitted, and full results are in **Supplementary Figure 9b**. **c** and **d**. The mean causal variant enrichment for GWAS within SCENT enhancers (green), all cis-ATAC peaks (yellow), ENCODE cCREs (pink), EpiMap enhancers across all groups (red) and ABC enhancers across all samples (blue). GWAS results were based on FinnGen (**c**) and UK Biobank (**d**). The bars indicate 95% confidence intervals by bootstrapping traits. **e**. The mean causal variant enrichment for FinnGen GWAS within intersection of SCENT enhancers and caQTL enhancers at each threshold of significance. The bars indicate 95% confidence intervals by bootstrapping traits.

283 We next compared the enrichment for eQTL putative causal variants in SCENT peaks to
284 peaks identified by the two published linear parametric methods using single-cell multimodal
285 data, ArchR[56] and Signac[50] using the same dataset. ArchR and Signac peaks had substantially
286 lower causal variant enrichment for eQTL (1.4X and 9.3X, respectively) compared to SCENT
287 peaks (74.1X) with FDR<0.10. We were concerned that this performance differences may reflect
288 variable recall; that is SCENT may be more restrictive and calling fewer peaks. By varying the
289 thresholds to define significant peak-gene associations (see **Methods**), we called the number of
290 peak-gene pairs with difference levels of stringency and tested causal variant enrichment (i.e.,
291 recall-precision tradeoff; **Figure 3b** and **Supplementary Figure 9b**). SCENT peaks consistently
292 demonstrated higher causal variant enrichment (i.e., precision) than ArchR and Signac peaks
293 across different recall values.

294 We also tested Cicero[51], which is a published linear parametric method for detecting
295 promoter-enhancer co-accessibility from ATAC-seq data alone. We confirmed that SCENT
296 peaks demonstrated higher causal variant enrichment than Cicero using the same dataset but
297 only with ATAC-seq side (**Supplementary Figure 9c;** see **Methods**).

298 We assessed whether the Poisson regression or the bootstrapping in SCENT was driving
299 its performance over other linear parametric methods. We benchmarked causal variant
300 enrichment in SCENT peaks against peaks identified with only Poisson regression but without
301 non-parametric bootstrapping (see **Methods**). As previously mentioned, we already observed
302 false positive associations in the simulated null datasets in the Poisson-only strategy
303 (**Supplementary Figure 1c**). Indeed, we observed substantially lower causal variant enrichment

304 at a given recall compared to SCENT (14.4X in Poisson only vs. 74.1X in SCENT at the same
305 FDR<0.10), albeit slightly higher than the linear methods ArchR and Signac (**Supplementary**
306 **Figure 9c**). This underscored the importance of accounting for both (1) sparsity by Poisson
307 regression and (2) highly variable gene count distribution by non-parametric bootstrapping to
308 achieve high precision in SCENT.

309 SCENT can detect *cis*-regulatory regions in a cell-type-specific manner. We created cell-
310 type-specific enhancer-gene maps in four major cell types with > 5,000 cells across datasets;
311 for each cell type we took the union of SCENT enhancers across datasets. The cell-type-specific
312 SCENT enhancers (e.g., SCENT B cell peaks) were most enriched in putative causal eQTL
313 variants within relevant samples in GTEx (e.g., EBV-transformed lymphocytes; **Supplementary**
314 **Figure 9d**).

315 These results suggest that SCENT can prioritize regulatory elements harboring putative
316 causal eQTL variants in a cell-type-specific manner, with higher precision than the previous
317 single-cell methods.

318

319 *Enrichment of likely causal variants for GWAS in SCENT enhancers*

320 SCENT applied for multimodal data from disease-relevant tissues can build disease-specific
321 enhancer-gene maps. We sought to examine whether SCENT peaks can be used for the more
322 difficult task of prioritizing disease causal variants. We obtained candidate causal variants for
323 diseases and traits from fine-mapping results of GWASs in two large-scale biobanks (PIP>0.2;
324 FinnGen[71] [1,046 disease traits] and UK Biobank[72] [35 binary traits and 59 quantitative traits])[28].

325 We computed enrichment statistics for causal GWAS variants within SCENT enhancers (both
326 cell-type-specific tracks and aggregated tracks across cell types; see **Methods**). The SCENT
327 enhancers were strikingly enriched in causal GWAS variants in FinnGen (31.6X on average;
328 1046 traits; **Figure 3c** and **Supplementary Figure 10a**) and UK Biobank (73.2X on average; 94
329 traits; **Figure 3d** and **Supplementary Figure 10b**). This enrichment was again much larger than
330 all *cis*-ATAC peaks (12.8X in FinnGen and 38.8X in UK Biobank). Moreover, the target genes of
331 the likely causal variants for autoimmune diseases (AID) identified by SCENT peaks in immune-
332 related cell types had higher fraction (10.8%) of know genes implicated in Mendelian disorders
333 of immune dysregulation (n_{gene} = 550)[73,74] than SCENT peaks in fibroblast (3.8%;
334 **Supplementary Figure 10c**).

335 We compared SCENT to alternative genome annotations and enhancer-gene maps from
336 bulk tissues. Causal variant enrichment in SCENT was much higher than the conventional bulk-
337 based annotations such as ENCODE cCREs (13.9X in FinnGen and 46.5X in UK Biobank), ABC
338 (16.3X in FinnGen and 53.3X in UK Biobank) and EpiMap (12.9X in FinnGen and 40.6X in UK
339 Biobank; **Figure 3c** and **3d** [aggregated tracks]**, Supplementary Figure 10a** and **10b** [cell-type-
340 specific tracks]**)**. We again assessed recall and precision tradeoffs by varying thresholds for
341 defining significant peak-gene linkages. We constructed SCENT from 9 datasets and 23 cell
342 types with only 28 samples, substantially less than the 833 samples and tissues used to
343 construct EpiMap and 131 samples and cell lines for the ABC model. Despite the smaller data
344 set, SCENT peaks consistently demonstrated higher precision (i.e., enrichment of causal GWAS
345 variants) at a given recall (i.e., a similar number of identified peak-gene linkages) than ABC

346 model and EpiMap (**Supplementary Figure 11a**). A more stringent PIP threshold (0.5 and 0.7)
347 for putative causal variants increased the enrichment while maintaining the higher enrichment in
348 SCENT than bulk methods (**Supplementary Figure 11b**). The target genes for AID by SCENT
349 in immune-related cell types had higher fraction (10.8%) of known Mendelian genes of immune
350 dysregulation[73,74] than EpiMap (8.6%) and ABC model (4.4%) (**Supplementary Figure 10c**).
351 These results demonstrate the power SCENT achieved by accurately modeling association
352 between chromatin accessibility and gene expression at the single-cell resolution.

353 We hypothesized that putative causal variants by SCENT would likely modulate
354 chromatin accessibility (e.g., transcription factor binding affinity). If so, the intersection of the
355 SCENT enhancers and chromatin accessibility quantitative trait loci (caQTL) could further enrich
356 the causal GWAS variants[75–78], because these intersected enhancers should include genetic
357 variants that directly change both chromatin accessibility and gene expression. To test this
358 hypothesis, we used single-cell ATAC-seq samples with genotype (n_{donor} = 17; arthritis-tissue
359 dataset) and performed caQTL mapping by leveraging allele-specific (AS) chromatin
360 accessibility (binomial test followed by meta-analysis across donors) or by combining AS with
361 inter-individual differences (RASQUAL[79]). We then intersected the caQTL ATAC peaks with the
362 SCENT enhancers and calculated the causal variant enrichment within these intersected regions.
363 We observed higher enrichment within intersected regions with SCENT and caQTL than those
364 with SCENT alone. The enrichment increased as we used more stringent threshold for caQTL
365 peaks, reaching as high as 333-fold when compared with background *cis*-regions (**Figure 3e**).
366 Thus, SCENT efficiently prioritized causal GWAS variants in part by capturing regulatory regions

367 of which chromatin accessibility is perturbed by genetic variants and modulates gene expression.
368 SCENT demonstrated a potential to further enrich causal variants by caQTLs if multimodal data
369 has matched genotype data.
370
371 *Defining mechanisms of GWAS loci by SCENT*
372 We finally sought to use SCENT enhancer-gene links to define disease causal mechanisms. We
373 analyzed the fine-mapped variants from GWASs (FinnGen, UK Biobank and GWAS cohorts of
374 rheumatoid arthritis (RA)[26], inflammatory bowel disease[29] and type 1 diabetes (T1D)[80]). SCENT
375 linked 4,124 putative causal variants (PIP>0.1) to their potential target genes across 1,143 traits
376 (**Supplementary Table 4**). These target genes were mostly close to the causal variant, with
377 20% of them being the closest gene to the causal variant (**Supplementary Figure 12a** and **12b**;
378 see **Methods**). However, 30.6% of the time SCENT linked causal variants to genes more than
379 300 kb away.
380 We first focus on autoimmune loci, given that our current SCENT tracks are largely
381 derived from immune cell types. We prioritized a single well fine-mapped variant rs72928038
382 (PIP > 0.3) at 6q15 locus in multiple autoimmune diseases (RA, T1D, atopic dermatitis and
383 hypothyroidism), within the T-cell-specific SCENT enhancer (T cells in Public PBMC and
384 Dogma-seq datasets; **Figure 4a**). This enhancer was linked to *BACH2*, which was also the
385 closest gene to this fine-mapped variant. Notably, base-editing in T cells has confirmed that this
386 variant affects *BACH2* expression[81]. Moreover, editing of this variant into CD8 T cells skewed
387 naive T cells toward effector T cell fates[81].
388

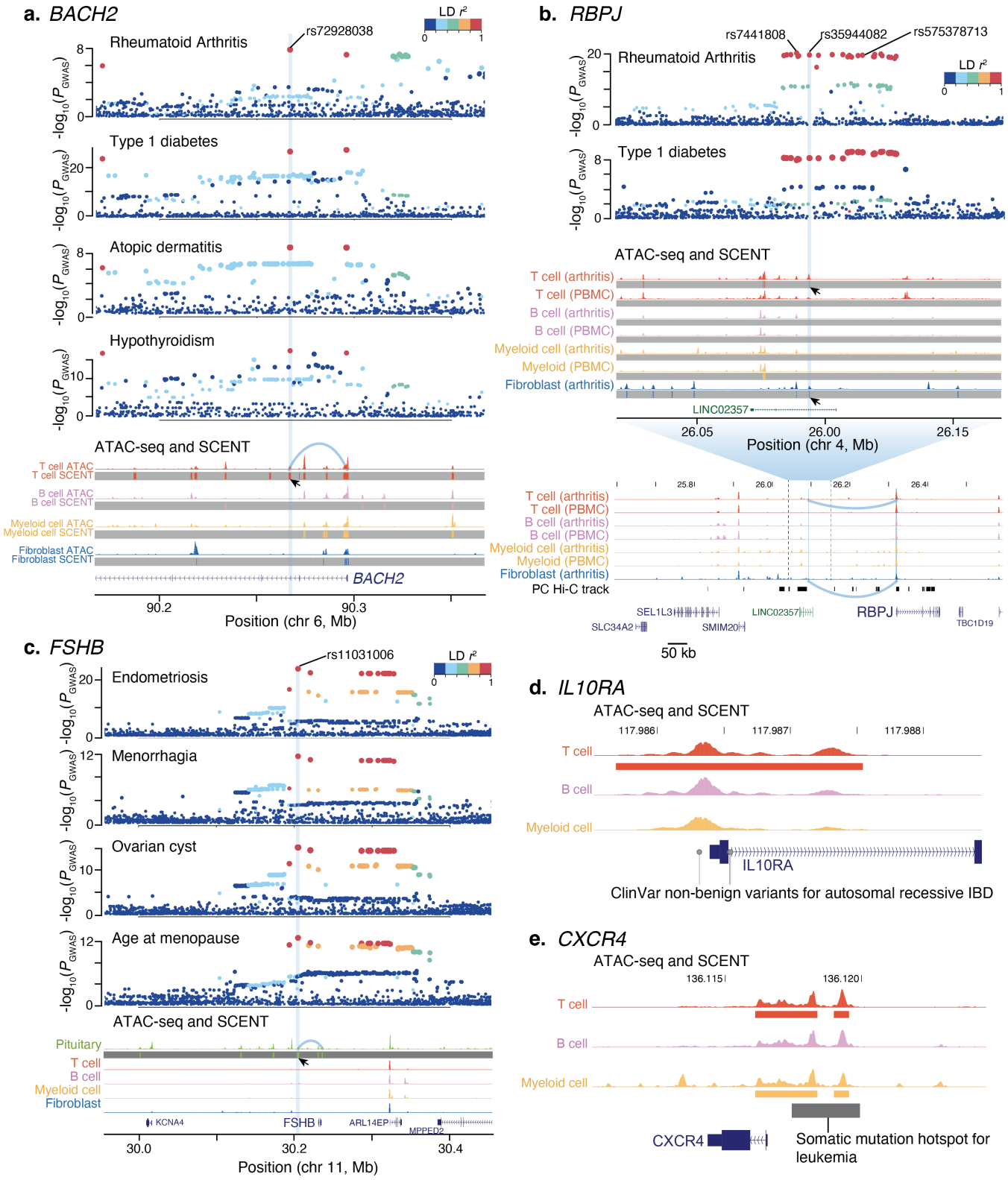

Figure 4. SCENT defined causal variants and genes in complex trait GWAS.
a. Rs72928038 at *BACH2* locus was prioritized by T-cell-specific SCENT enhancer-gene map, being for RA, T1D, Atopic dermatitis and hypothyroidism. The top four panels are GWAS regional

plots, with x-axis representing the position of each genetic variant. The color of the dots represent LD r^2 from the prioritized variant (highlighted by light blue stripe). ATAC-seq and SCENT tracks represent aggregated ATAC-seq tracks (top) and SCENT peaks (bottom with grey stripes) in each cell type (public PBMC dataset for immune cell types and arthritis-tissue dataset for fibroblast). An arrow head indicates the SCENT peak overlapping with fine-mapped variant. **b**. Rs35944082 for RA and T1D was prioritized and connected to *RBPJ* by long-range interaction from T-cell- and fibroblast- SCENT enhancer-gene map using inflamed synovium in arthritis-tissue dataset. The top two panels are GWAS regional plots similarly to panel **a**. ATAC-seq and SCENT tracks are shown similarly to panel **a**, but using both public PBMC and arthritis-tissue datasets. **c**. Rs11031006 was prioritized and connected to *FSHB* for multiple gynecological traits by using pituitary-derived single-cell multimodal dataset. The top four panels are GWAS regional plots similarly to panel **a**. ATAC-seq and SCENT tracks are shown similarly to panel **a**, and include tracks from pituitary dataset. There were no SCENT peaks in cell types except for pituitary. **d**. ATAC-seq and SCENT tracks for *IL10RA* locus, where non-coding ClinVar variants (grey dots) colocalized with T-cell SCENT track. **e**. ATAC-seq and SCENT tracks for *CXCR4* locus, where somatic mutation hotspot for leukemia colocalized with T-cell and myeloid-cell SCENT tracks.

410 Another locus for RA and T1D at 4p15.2 harbored 21 candidate variants, each with low
411 PIPs (< 0.14). SCENT prioritized a single variant rs35944082 in T cells and fibroblasts only within
412 the arthritis-tissue dataset from inflamed synovial tissue (**Figure 4b**). SCENT linked this variant
413 to *RBPJ*, which was the 3rd closest gene to this variant located 235kb away. This variant-gene
414 link was supported by a physical contact from promotor-capture Hi-C data in hematopoietic
415 cells[82]. *RBPJ* (recombination signal binding protein for immunoglobulin kappa J region) is a
416 transcription factor critical for NOTCH signaling, which has been implicated in RA tissue
417 inflammation through functional studies[83,84]. *Rbpj* knockdown in mice resulted in abnormal T cell
418 differentiation and disrupted regulatory T cell phenotype[85,86], consistent with a plausible role in
419 autoimmune diseases. Intriguingly, we observed no SCENT peaks in T cells from PBMC or blood
420 at this locus. This linkage was not present in EpiMap. ABC map prioritized another variant,
421 rs7441808 at this locus and linked it non-specifically to 16 genes including *RBPJ*, making it
422 difficult to define the true causal gene. These results underscored the importance of creating
423 enhancer-gene links using causal cell types, in this case cells from inflammatory tissues, in the
424 instances where links exist only in disease-relevant tissues.

425 We highlight another example of SCENT to build enhancer-gene maps from disease-
426 critical tissues. We examined the enhancer-gene map produced from single-cell pituitary data[62]
427 to assess 11p14.1 locus for multiple gynecological traits (endometriosis, menorrhagia, ovarian
428 cyst and age at menopause). Our map connected rs11031006 to *FSHB* (follicle stimulating
429 hormone subunit beta) (**Figure 4c**), which is specifically expressed in the pituitary[70,87] and
430 enables ovarian folliculogenesis to the antral follicle stage[88]. Rare genetic variants within *FSHB*

431 cause autosomal recessive hypogonadotropic hypogonadism[89]. However, multimodal data from
432 other tissues and bulk-based methods (ABC model and EpiMap) were unable to prioritize this
433 variant, since they missed the most disease-relevant tissue of pituitary.
434
435 *Mendelian-disease variants and somatic mutations in cancer within SCENT enhancers*
436 Having established the SCENT's utility in defining likely causal variants and genes in complex
437 diseases, we examined rare non-coding variants causing Mendelian diseases. Currently, causal
438 mutations and genes can only be identified in ~30–40% of patients with Mendelian diseases[90–
439 92]. Consequently, many variants in cases are annotated as variants of uncertain significance
440 (VUS). The VUS annotation is especially challenging for non-coding variants. We examined the
441 overlap of clinically reported non-benign non-coding variants by ClinVar[93] (400,300 variants in
442 total) within SCENT enhancers. The SCENT enhancers harbored 2.0 times ClinVar variants on
443 average than all the ATAC regions with the same genomic length across all the datasets
444 (**Supplementary Figure 13**). This density of ClinVar variants was 3.2 times and 12 times on
445 average larger than that in ENCODE cCREs and of all non-coding regions, respectively. We
446 defined 3,724 target genes for 33,618 non-coding ClinVar variants by SCENT in total
447 (**Supplementary Table 5**). As illustrative examples, we found 40 non-coding variants linked to
448 *LDLR* gene causing familial hypercholesterolemia 1[93], 3 non-coding variants linked to *IL10RA*
449 causing autosomal recessive early-onset inflammatory bowel disease 28 (**Figure 4d**)[94], and an
450 intronic variant rs1591491477 linked to *ATM* gene causing hereditary cancer-predisposing
451 syndrome[93].

452 Finally, we used SCENT to connect non-coding somatic mutation hotspots to target genes.
453 Recently, somatic mutation analyses across the entire cancer genome revealed possible driver
454 non-coding events[95]. Among 372 non-coding mutation hotspots in 19 cancer types, SCENT
455 enhancers included 193 cancer-mutation hotspot pairs (**Supplementary Table 6**). SCENT
456 enhancer-gene linkage successfully linked those hotspots to known driver genes (e.g., *BACH2*,
457 *BCL6*, *BCR*, *CXCR4* (**Figure 4e**), and *IRF8* in leukemia). In some instances, SCENT nominated
458 different target genes for these mutation hotspots from those based on ABC model used in the
459 original study. For example, SCENT connected a somatic mutation hotspot in leukemia at
460 chr14:105568663-106851785 to *IGHA1* (Immunoglobulin Heavy Constant Alpha 1), which might
461 be more biologically relevant than *ADAM6* nominated by ABC model. These results implicate
462 broad applicability of SCENT for annotating all types of human variations in non-coding regions.
463

464 *Augmenting SCENT enhancer-gene maps with more samples*

465 While the recall for enhancer-gene maps defined by SCENT was lower than that by bulk-tissue-
466 based methods, this might be a function of current limited sample sizes. We assessed if the
467 addition of more cells into SCENT leads to the higher recall for enhancer-gene maps while
468 retaining the precision. By downsampling of our multimodal single cell dataset, we observed that
469 the number of significant gene-peak pairs increased linearly to the number of cells per cell type
470 in a given dataset, suggesting that SCENT will be even better powered as the size of sc-
471 multimodal datasets increases (**Supplementary Figure 14**). We considered the possibility that
472 enhancer-gene maps with greater numbers of cells might capture spurious associations; if this

was the case, we would expect more long-range associations, which are more likely to be false positives with greater cell numbers. In contrast, shorter-range and longer-range associations were both equivalently represented as we added cells, suggesting the robustness of our discovery.

Discussion

In this study, we presented a novel statistical method, SCENT, to create a cell-type-specific enhancer-gene map from single-cell multimodal data. Single-cell RNA-seq and ATAC-seq are both sparse and have variable count distributions, which requires non-parametric bootstrapping to connect chromatin accessibility with gene expression. The SCENT model demonstrated well-controlled type I error, outperforming commonly used statistical models which showed inflated statistics. SCENT mapped enhancers that showed strikingly high enrichment for putative causal variants in eQTLs and GWASs and outperformed previous methods for single-cell multimodal data (e.g., ArchR[49] and Signac[50]). Despite using substantially lower number of samples (28 from 9 datasets in total), enhancers defined by SCENT had equivalent or even higher enrichment for putative causal variants than bulk-tissue-based methods with more than 100 samples (e.g., EpiMap and ABC model), by modeling single-cell level observations instead of obscuring them into sample-level association.

As potential limitations, first, our enhancer-gene maps had relatively fewer enhancers (lower recall) compared to other resources (**Figure 2a**). However, downsampling experiments

494 showed a clear linear relationship between the number of cells and the number of significant
495 SCENT peak-gene links. It follows that SCENT applied to larger datasets from a diverse set of
496 tissues will further expand the current enhancer-gene map. In contrast, bulk-tissue-based
497 enhancer-gene map might have an upper limit of discovery by the number of samples generated
498 by each consortium (e.g., ENCODE). Second, SCENT focuses on gene *cis*-regulatory
499 mechanisms to fine-map disease causal alleles, while there could be other causal mechanisms
500 that explain disease heritability, such as alleles that act through *trans*-regulatory effects, splicing
501 effects, or post-transcriptional effects[96].

502 We argue that the real utility of SCENT is that it enables the construction of disease-
503 tissue-relevant enhancer-gene maps. Multimodal single cell data can be easily obtained from a
504 wide range of primary human tissues. Since these assays query nuclear material, data can be
505 obtained without disaggregating tissues and thus can be employed for assays that need intact
506 cells from tissue. Therefore, it is possible to build relevant tissue-specific enhancer-gene maps
507 that are necessary to understand the causal mechanisms of common diseases, rare diseases,
508 and somatic non-coding mutations in cancers. For example, understanding the *FSHB* locus in
509 gynecological traits specifically required a pituitary map, and *RBPJ* locus in RA specifically
510 required a synovial tissue map.

511 In summary, our method SCENT is a robust, versatile method to efficiently define causal
512 variants and genes in human diseases and will fill the gap in the current enhancer-gene map
513 built from genomic data in bulk tissues.

514

515 **Data Availability**

516 The publicly available datasets were downloaded via Gene Expression Ombibus (accession
517 codes: GSE140203, GSE156478, GSE178707, GSE193240, GSE178453) or web repository
518 (https://www.10xgenomics.com/resources/datasets?query=&page=1&configure%5Bfacets%5D
519 %5B0%5D=chemistryVersionAndThroughput&configure%5Bfacets%5D%5B1%5D=pipeline.ve
520 rsion&configure%5BhitsPerPage%5D=500&menu%5Bproducts.name%5D=Single%20Cell%2
521 0Multiome%20ATAC%20%2B%20Gene%20Expression,
522 https://openproblems.bio/neurips_docs/data/dataset/). The raw data for arthritis-tissue dataset
523 (single-cell multimodal RNA/ATAC-seq and single-cell ATAC-seq) will be publicly available
524 before the acceptance of this manuscript.

525

526 **Code Availability**

527 The computational scripts related to this manuscript are available at
528 https://github.com/immunogenomics/SCENT.

529

530 **Methods**

531 *Data and sample in arthritis-tissue dataset*

532 This study was performed in accordance with protocols approved by the Brigham and Women's
533 Hospital and the Hospital for Special Surgery institutional review boards. Synovial tissue from
534 patients with RA and OA were collected from synovectomy or arthroplasty procedures followed
535 by cryopreservation as previously described[97]. RA samples with high levels of lymphocyte

536 infiltration (as scored by a pathologist on histologic sections) were identified as “inflamed” and
537 used for downstream analysis. Next, cryopreserved synovial tissue fragments were dissociated
538 by a mechanical and enzymatic digestion[97], followed by flow sorting to enrich for live synovial
539 cells. For each tissue sample, the viable cells were isolated and lysed to extract and load
540 approximately 10,000 nuclei according to manufacturer protocol (10X Genomics). Joint sc-RNA-
541 and sc-ATAC-seq libraries were prepared using the 10x Genomics Single Cell Multiome ATAC
542 + Gene Expression kit according to manufacturer’s instructions. Libraries were sequenced with
543 paired-end 150-bp reads on an Illumina Novaseq to a target depth of 30,000 read pairs per
544 nuclei both for mRNA and ATAC libraries. Demultiplexed scRNA-seq fastq files were inputted
545 into the Cell Ranger ARC pipeline (version 2.0.0) from 10x Genomics to generate barcoded
546 count matrix of gene expression. For ATAC-seq, we trimmed adaptor and primer sequences and
547 mapped the trimmed reads to the hg38 genome by BWA-MEM with default parameters. To
548 deduplicate reads from PCR amplification bias within a cell while keeping reads originating from
549 the same positions but from different cells, we used in-house scripts (manuscript in preparation).
550

551 *Uniform processing of single-cell multimodal datasets*

552 In addition to our arthritis-tissue multimodal dataset, we downloaded all publicly available
553 multimodal RNA-seq/ATAC-seq datasets from adult human tissues (n_{dataset} = 9, as of April 2022).
554 We processed these downloaded count matrices of gene expression and ATAC data. Briefly,
555 we applied QC to both the nuclear RNA data and the ATAC data based on RNA counts, ATAC
556 fragments, nucleosome signal, and TSS enrichment (**Supplementary Table 7**). We only kept

557 cells that had passed QC in both RNA-seq and ATAC-seq. Then to identify open chromatin
558 regions (peaks), we used macs2 to call open chromatin peaks using post-QC ATAC-seq data.
559 We thus obtained count matrices of gene expression and ATAC peaks with corresponding cell
560 barcodes. Gene expression counts were normalized using the NormalizeData function
561 (Seurat[98]), scaled using the ScaleData function (Seurat), and batch corrected using Harmony[99].
562 We visualized the cells in two low-dimensional embeddings with UMAP by using 20 batch-
563 corrected principal components from these normalized gene expression matrices (**Figure 1c**).
564 When original cell labels are provided by the authors, we used those labels to obtain broad cell
565 type categories. When they are not available, we performed reference-query mapping by Seurat
566 and PBMC reference object to define broad cell type labels. ATAC peak matrix was binarized to
567 have 1 if a count is > 0 and 0 otherwise.

568

569 *SCENT method*

570 We defined *cis*-peaks as any peaks whose center is within the window +/-500 kb from a given
571 gene body. We modeled the association between peak's binarized accessibility and the target
572 gene's expression with Poisson distribution:

573 $$E_i \sim Poisson(\lambda_i)$$

574 $$log(\lambda_i) = \beta_0 + \beta_{peak}X_{peak} + \beta_{\%mito}X_{\%mito} + \beta_{nUMI}X_{nUMI} + \beta_{batch}X_{batch} \quad (Equation\ 1)$$

575 where E_i is the observed expression count of ith gene, and λ_i is the expected count under
576 Poisson distribution. β_{peak} indicates the effect of chromatin accessibility of a peak on i th gene
577 expression. $\beta_{\%mito}$, β_{nUMI}, and β_{batch} each represents the effect of covariates, percentage of

578 mitochondrial reads per cell as a mesure of cell quality, the number of UMIs in the cell, and the
579 batch, respectively. To empirically assess error and significance of β_{peak} for each peak-gene
580 combination, we used bootstrapping procedures. In brief, we resampled cells with replacement
581 in each bootstrapping procedure and re-estimated β'_{peak} within those resampled cells. We
582 repeated this procedure *N* times, where we adaptively increased *N* (i.e., the total number of
583 bootstrapping) from at least 100 and up to 50,000, depending on the significance of β_{peak} (as
584 described next) in each chunk of bootstrapping trials to reduce the computational burden. After
585 *N* times of bootstrapping, we assessed the distribution of *N* β'_{peak}s against null hypothesis
586 (β'_{peak} = 0) to derive the significance of β_{peak} (i.e., two-sided bootstrapping-based *P* value for
587 this peak-gene combination by counting the instances where the statistics are equal or more
588 extreme than the null hypothesis of β'_{peak} = 0; **Supplementary Figure 2**).

589 To avoid spurious associations from rare ATAC peak and rare gene expression, we QCed
590 cis-peak-gene pairs we test so that both peak and gene should have been expressed in at least
591 5% of the cells we analyze. We finally defined a set of significant peak-gene pairs for each cell
592 type based on bootstrapping-based *P* values and FDR correction for multiple testing (Benjamini
593 & Hochberg correction).

594 When we tested the calibration of statistics from SCENT or other regression strategies
595 (**Supplementary Figure 1**), we used null dataset where we randomly permuted cell labels in the
596 ATAC-seq and ran the regression model we tested.

597

598 *ArchR peak2gene and Signac LinkPeaks method*

599 We analyzed arthritis-tissue dataset with ArchR[49] and Signac[50] for single-cell multimodal data,
600 which both have a function to define peak-gene linkages. In brief, ArchR takes multimodal data
601 and creates low-overlapping aggregates of single cells based on *k*-nearest neighbor graph. Then
602 it correlates peak accessibility with gene expression by Pearson correlation of aggregated and
603 log2-normalized peak count and gene count. Signac computes the Pearson correlation
604 coefficient *r* (corSparse function in R) for each gene and for each peak within 500kb of the gene
605 TSS. Signac then compares the observed correlation coefficient with an expected correlation
606 coefficient for each peak given the GC content, accessibility, and length of the peak. Signac
607 defines *P* value for each gene-peak links from the z score based on this comparison. We ran
608 both methods on arthritis-tissue dataset with default parameters. We output statistics for all
609 peak-gene pairs we tested without any cut-off for correlation *r* or *P* values. We used FDR in the
610 output from ArchR software, or computed FDR using *P* values in the output from Signac software
611 by Benjamini & Hochberg correction. We defined significant peak-gene linkages as those with
612 FDR < 0.10, and used varying correlation *r* to assess the precision and recall in the causal variant
613 enrichment analysis (see later sections in **Method**).
614

615 *Replication across datasets*

616 Since we have the same immune-related cell types across different multimodal datasets, we
617 evaluated the concordance of enhancer-gene map in a discovery dataset (arthritis-tissue
618 dataset) when compared with other replication datasets including immune-related cell types
619 (Public PBMC, NeurIPS, SHARE-seq and NEAT-seq datasets). To this end, we used most

stringent FDR threshold for defining an enhancer-gene map in arthritis-tissue dataset (FDR < 1%). We then used more lenient threshold for defining an enhancer-gene map in replication datasets (FDR < 10%), which is a similar strategy used in assessing replication in GWAS. For each cell type and for each replication dataset, we took the intersection of enhancer-gene links defined as significant in both datasets. We assessed the directional concordance (i.e., concordance of the sign of β_{peak}) and the Pearson's correlation *r* of β_{peak} between the discovery and the replication for these peak-gene pairs. For the largest replication dataset of Public PBMC, we performed the same analysis for enhancer-gene map from ArchR and Signac software.

Conservation score analysis

To compare the evolutional conservation across species between our annotated peaks and the other peaks, we used phastCons[66] score. We downloaded the phastCons score for multiple alignments of 99 vertebrate genomes from https://hgdownload.cse.ucsc.edu/goldenpath/hg19/phastCons100way/. We lifted them over to GRCh38 by LiftOver software. We used SCENT results for arthritis-tissue, Public PBMC and NeurIPS for conservation score analysis as representative datasets with the largest numbers of cells. Because each gene should have variable functional importance and conservation, we assessed each gene separately. For each gene, we took (1) an annotation of interest for the gene and (2) all *cis*-non-coding regions (< 500kb from a gene), and computed the mean phastCons score of each of two sets of the peaks. As annotations to be tested, we used a. exonic

regions of the gene, b. SCENT peaks for the gene, and c. all ATAC peaks in cis-regions from the gene (< 500 kb). Then, we took the difference between two mean differences ($\Delta\,\mathrm{phastCons\ score}$), and computed the mean differences across all the genes ($\mathrm{mean}\ \Delta\ \mathrm{phastCons\ score}$) as follows.

$$\mathrm{mean}\ \Delta\ \mathrm{phastCons\ score} = \frac{1}{n_{gene}} \sum_{gene} \left(\overline{phastCons}_{g,in_annot} - \overline{phastCons}_{g,non-coding}\right)$$

By bootstrapping the genes, we calculated the 95% CI of the mean Δ phastCons score. If this metric is positive, that indicates that the annotated regions are more conserved than non-coding regions.

We also calculated similar Δ phastCons score by comparing the SCENT peaks with TSS-distance-matched non-SCENT peaks in each dataset.

$$\mathrm{mean}\ \Delta\ \mathrm{phastCons\ score} = \frac{1}{n_{gene}} \sum_{gene} \left(\overline{phastCons}_{g,peak_in_SCENT} - \overline{phastCons}_{g,peak_non_SCENT_matched}\right)$$

By bootstrapping the genes, we again calculated the 95% CI of the mean Δ phastCons score. If this metric is positive, that indicates that SCENT peaks are more conserved than TSS-distance-matched non-SCENT peaks.

Construction of a set of TSS-matched non-SCENT peaks

To assess the effect of TSS distance when comparing SCENT peaks with non-SCENT peaks, we matched each one of the SCENT peak-gene pairs to one non-SCENT peak-gene pair, where the peak had the most similar TSS distance to the same gene among all the ATAC peaks in *cis* in each of the dataset. We confirmed that the resulting TSS-distance-matched non-SCENT

peak-gene pairs demonstrated the similar distributions of TSS distance when compared with the SCENT peak-gene pairs (**Supplementary Figure 6b**).

Gene's constraint and the number of significant SCENT peaks for a gene

We sought to investigate the relationship between the number of significant SCENT peaks for each gene and the gene's evolutionary constraint. We used pLI and LOEUF as metrics for the gene's loss-of-function intolerance within human population. We downloaded both pLI and LOEUF scores from gnomAD browser (https://gnomad.broadinstitute.org/downloads). We inverse-normal transformed the raw number of significant SCENT peaks for each gene, since the raw number of significant SCENT peaks for each gene is skewed toward zero (**Supplementary Figure 5a**). We performed linear regression between the normalized number of significant SCENT peaks and pLI or LOEUF score with accounting for gene length, which could be potential confounding factor for pLI and LOEUF[67,68].

Validation with CRISPR-Flow FISH results

To validate our SCENT enhancer-gene links, we used published CRISPR-Flow FISH experiments as potential ground-truth positive enhancer element-gene links and negative enhancer element-gene links. We downloaded the experimental results from the **Supplementary Table 5** of original publication[39]. We used "Perturbation Target" as candidate enhancer elements. We defined 283 positive enhancer element-gene links when they are "TRUE" for "Regulated" column (i.e., the element-gene pair is significant and the effect size is negative)

683 and 5,472 negative enhancer element-gene links when they are “FALSE” for “Regulated” column.
684 We lifted them over to GRCh38 and obtained final sets of 278 positive links and 5,470 negative
685 links.

686 We used two most powered datasets, arthritis-tissue and Public PBMC datasets. For
687 each dataset, we used “bedtools intersect” to categorize SCENT peak-gene links and non-
688 SCENT ATAC peak-gene pairs into either CRISPR-positive or CRISPR-negative groups, based
689 on whether these peaks overlapped with positive or negative CRISPR-Flow FISH links for the
690 same gene (**Supplementary Table 3**). We finally performed two-sided Fisher’s exact test to
691 assess the enrichment of CRISPR-positive links within SCENT peak-gene links in each dataset.
692

693 *Cell-type-specific SCENT tracks and aggregated SCENT tracks*

694 For cell types with more than 5,000 cells across datasets, we concatenated SCENT peak-gene
695 linkages across all the datasets to create cell-type-specific SCENT tracks. We collected a set of
696 SCENT peak-gene linkages for the same cell type and used “bedtools merge” function (for each
697 gene) to obtain a union of SCENT peaks for each gene. Similarly, we created aggregated
698 SCENT tracks across all the cell types and all datasets. We collected all sets of SCENT peak-
699 gene linkages and used “bedtools merge” function (for each gene) to obtain a union of SCENT
700 peaks for each gene across all the cell types and all datasets.
701

702 *Causal variant enrichment analysis using eQTLs*

703 We defined a causal enrichment for eQTL within SCENT enhancers and other annotations by
704 using statistically fine-mapped variant-gene combinations from GTEx. We used publicly
705 available statistics analyzed by CAVIAR software[20], and selected variants with PIP > 0.2 as
706 putatively causal (fine-mapped) variants for primary analyses. For the primary enrichment
707 analysis, we aggregated fine-mapped variants from all the 49 tissues. For cell-type-specific
708 SCENT enrichment analysis (**Supplementary Figure 9d**), we used fine-mapped variants from
709 each tissue separately. We intersected these putatively causal variants with our annotation
710 (SCENT peaks, ArchR peaks or Signac peaks). We then retained any variants which the linking
711 method (SCENT, ArchR, Signac, and Cicero) connected to the same gene as GTEx phenotype
712 gene.

713 $$Enrichment_{gene_i} = \frac{\#\, causal_var_in_annot_{gene_i} \Big/ \sum common_var_in_annot_{gene_i}}{\#\, causal_var_{gene_i} \Big/ \sum common_var_in_cis_{gene_i}}$$

714

715 $$Overall_Enrichment = \frac{1}{n}\sum_{i=1}^{n} Enrichment_{gene_i}$$

716 For each gene i (expression phenotype), we divided the number of putatively causal variants
717 within an annotation normalized by the number of common variants within an annotation by the
718 number of all causal variants for gene i normalized by the number of all common variants within
719 cis-region from for gene i. To calculate common variants within annotation or within locus, we
720 used 1000 Genomes Project genotype. We selected any variants with minor allele frequency >
721 1% in European population as a set of common variants to be intersected with each annotation.
722 To derive $Overall_Enrichment$ score, we took the mean across all the genes.

723 To have further insights into precision and recall and compare against ArchR peak2gene
724 and Signac LinkPeaks functions, we varied the threshold for defining a set of significant peak-
725 gene linkages in each software (i.e., FDR in SCENT {0.50, 0.30, 0.20, 0.10, 0.05, 0.02},
726 Peason's correlation *r* {any, 0, 0.1, 0.3, 0.5, 0.7} in ArchR, and correlation socre {any, 0, 0.05,
727 0.1, 0.15} in Signac). We used the same myeloid cells in the arthritis-tissue dataset and a set of
728 eQTL fine-mapped variants in GTEx blood tissue for this benchmark across all three methods.
729 We then used each set of peak-gene linkages to re-calculate causal variant enrichment
730 $Overall_Enrichment$ score (**Figure 3b**).
731 We also assessed the impact of PIP threshold in defining a set of statistically fine-mapped
732 variants on the causal variant enrichment analysis. To do so, we re-defined the set of putative
733 causal variants with more stringent PIP thresholds (PIP > 0.5 and PIP > 0.7), and re-computed
734 the calculate causal variant enrichment $Overall_Enrichment$ score.
735

736 *Cicero co-accessibility analyses*

737 To benchmark our SCENT using single-cell multimodal ATAC/RNA-seq against a published
738 method using single-cell unimodal ATAC-seq alone, we ran Cicero[51] for the same dataset of
739 myeloid cells in the arthritis-tissue dataset as benchmarked in the SCENT, ArchR and Signac.
740 We only used the peak by cell matrix from the ATAC-seq side of the arthritis-tissue dataset and
741 ran "run_cicero" function with default parameters to obtain Cicero co-accessibility scores. We
742 only retained peak-peak co-accessibility as potential enhancer-gene connection when one of the
743 co-accessible peaks is a promoter of a gene (defined by the peak's distance to the TSS < 1kb);

744 we treated them as putative enhancer-gene (promoter) linkage. We used the co-accessibility
745 scores {any, 0, 0.1, 0.3, 0.4, 0.5, 0.7} for assessing the recall-precision tradeoffs as described in
746 the previous section.
747
748 *Peak-gene linkage using Poisson regression alone*
749 As other benchmarking for assessing the effect of the components of SCENT on the causal
750 variant enrichment, we also created peak-gene linkage using the Poisson regression but without
751 non-parametric bootstrapping for the same dataset of myeloid cells in the arthritis-tissue dataset.
752 We used the nominal *P* values for the term X_{peak} from the Poisson regression ($Equation\ (1)$) to
753 perform FDR correction to obtain significant peak-gene pairs using the Poisson regression alone. We
754 then used the FDR thresholds {0.30, 0.20, 0.10, 0.05, 0.02, 0.01} for assessing the recall-precision
755 tradeoffs as described in the previous section.
756
757 *GWAS fine-mapping results*
758 We used GWAS fine-mapping results in FinnGen release 6[71] upon registration and publicly
759 available GWAS fine-mapping results in UK Biobank[72] (https://www.finucanelab.org/data). For
760 FinnGen traits, we downloaded all the fine-mapping results by SuSIE software[22] and
761 systematically selected any traits with case count > 1,000. We then selected non-coding fine-
762 mapped loci which did not include any non-synonymous or splicing variants with PIP > 0.5. We
763 thus analyzed 1,046 traits and 5,753 loci in total after QC. For UK Biobank, we analyzed the
764 fine-mapping results by SuSIE software for all 94 traits including binary and quantitative traits.

765 Since the genomic coordinates for the UK Biobank fine-mapping results were hg19, we lifted
766 them over to GRCh38 by using LiftOVer software. We again selected non-coding fine-mapped
767 loci which did not include any non-synonymous or splicing variants with PIP > 0.5. We thus
768 analyzed 7,274 loci in total after QC.

769 We analyzed three additional autoimmune GWAS fine-mapping results for RA[26], T1D[80],
770 and IBD[29], given our special interest in immune-mediated traits. We similarly selected non-
771 coding fine-mapped loci which did not include any non-synonymous or splicing variants with PIP
772 > 0.5, and lifted the results over to GRCh38 by using LiftOVer software. We defined 117 loci for
773 RA, 77 loci for T1D and 86 loci for IBD.

774

775 *Causal variant enrichment analysis using GWASs*

776 We defined a causal enrichment for GWAS within SCENT enhancers and other annotations by
777 using statistically fine-mapped variants from FinnGen[71] and UK Biobank[72] which we described
778 in the previous section. We selected variants with PIP > 0.2 as putatively causal variants for
779 primary analyses.

780 $$Enrichment_{trait_i} = \frac{\#\ causal_var_in_annot_{trait_i} \Big/ \sum common_var_in_annot_{trait_i}}{\#\ causal_var_{trait_i} \Big/ \sum common_var_across_loci_{trait_i}}$$

781

782 $$Overall_Enrichment = \frac{1}{n}\sum_{i=1}^{n} Enrichment_{trait_i}$$

783 For each trait i, we divided the number of putatively causal variants within an annotation (across
784 all loci for trait i) normalized by the number of common variants within an annotation by the

785 number of all causal variants for trait i normalized by the number of all common variants within
786 all significant loci analyzed for the trait i. To calculate common variants within annotation or
787 within locus, we again used 1000 Genomes Project variants with minor allele frequency > 1% in
788 European population. To derive $Overall_Enrichment$ score, we took the mean across all the
789 traits.

790 For each trait i and putative causal gene pair, we calculated the distance between the
791 TSS of the gene and the most likely causal variant which had the largest PIP when multiple
792 variants were nominated for a single gene by SCENT (**Supplementary Figure 12a**). For each
793 putative causal gene for the trait i, we also sorted all the genes based on the distance between
794 the gene's TSS and the most likely causal variant (from the smallest to the largest). We then
795 obtained the rank of the putative causal gene from SCENT among the sorted gene list to see
796 how often the SCENT gene is the closest gene from the most likely causal variant.

797

798 *Comparison with bulk-tissue-based regulatory annotation and enhancer-gene maps*

799 We downloaded per-group EpiMap enhancer-gene links from
800 https://personal.broadinstitute.org/cboix/epimap/links/pergroup/. We lifted the genomic
801 coordinates to GRCh38 by using LiftOver software. When we assessed aggregated EpiMap
802 enhancer-gene links across all the 31 tissue-groups, we used "bedtools merge" function for each
803 gene to create a union of all enhancer-gene links (**Figure 3c and d**). For tissue-specific
804 enrichment analyses, we analyzed the 31 group-specific tracks separately (**Supplementary**
805 **Figure 10a** and **10b**). To benchmark the precision and recall, we used EpiMap correlation scores

306 to define variable sets of enhancer-gene links from EpiMap based on the threshold of EpiMap
307 correlation score.

308 We downloaded ABC predictions in 131 cell types and tissues from
309 ftp://ftp.broadinstitute.org/outgoing/lincRNA/ABC/AllPredictions.AvgHiC.ABC0.015.minus150.F
310 orABCPaperV3.txt.gz. We lifted the genomic coordinates to GRCh38 by using LiftOver software.
311 When we assessed aggregated ABC enhancer-gene links across all the groups, we used
312 "bedtools merge" function for each gene to create a union of all enhancer-gene links across 131
313 cell types (**Figure 3c and d**). For cell-type-specific analyses, we aggregated cell lines or cell
314 types to be corresponding with our cell types and analyzed each of these tracks separately (B
315 cell, T cell, Myeloid cells, and fibroblasts; **Supplementary Figure 10a** and **10b**). To benchmark
316 the precision and recall, we used ABC scores to define variable sets of enhancer-gene links
317 from ABC model based on the threshold of ABC score.

318 To assess precision and recall and compare against bulk-tissue based methods (i.e.,
319 EpiMap and ABC model), we used sets of significant peak-gene linkages in each method with
320 varying thresholds (i.e., FDR in SCENT {0.5, 0.3, 0.2, 0.1, 0.05, 0.02}, EpiMap correlation score
321 {0, 0.4, 0.8, 0.9} in EpiMap, and ABC score {0, 0.05, 0.1, 0.2} for ABC model). We then used
322 each set of peak-gene linkages to re-calculate causal variant enrichment for GWAS (**Figure 3d**).

323 We also assessed the impact of PIP threshold in defining a set of statistically fine-mapped
324 variants on the causal variant enrichment analysis. To do so, we re-defined the set of putative
325 causal variants with more stringent PIP thresholds (PIP > 0.5 and PIP > 0.7), and re-computed
326 the calculate causal variant enrichment $Overall_Enrichment$ score.

327

328 *caQTL analysis using scATAC-seq samples with genotype*

329 We generated independent arthritis-tissue dataset with single-cell unimodal ATAC-seq data with
330 genotype (n = 17, *manuscript in preparation*) to define chromatin accessibility QTLs (caQTLs).
331 We used two methods, binomial test and RASQUAL. Briefly, we genotyped donors by using
332 Illumina Multi-Ethnic Genotyping Array. We performed quality control of genotype by sample call
333 rate > 0.99, variant call rate > 0.99, minor allele frequency > 0.01, and $P_{HWE} > 1.0\times10^{-6}$. We
334 performed haplotype phasing with SHAPEIT2 software[100] and performed whole-genome
335 imputation by using minimac3 software[101] with a reference panel of 1000 Genomes Project
336 phase 3[102]. After imputation, we selected variants with imputation *Rsq* > 0.7 as post-imputation
337 QC. We next created a merged bam file of ATAC-seq for each donor and each cell type by
338 aggregating all the reads. Using the imputed genotype for each donor and aggregated bam files
339 for each donor and cell type, we applied WASP[103] to correct any bias in read mapping toward
340 reference alleles to accurately quantify allelic imbalance. We thus created a bias-corrected bam
341 files for each donor and cell type.

342 For binomial tests, we ran ASEReadCounter module in GATK software[104] using the bias-
343 corrected bam files as input to quantify allelic imbalance in heterozygous sites with read count
344 > 4 within ATAC peak counts. We first performed one-sided binomial tests in each donor, and
345 meta-analyzed the statistics across donors by Fisher's method if multiple donors shared the
346 same heterozygous site. For RASQUAL, we created a VCF file containing both genotype dosage
347 and allelic imbalance from ASEReadCounter. We quantified the read coverage for each peak

348 and for each donor by “bedtools coverage” function. We created a peak by donor matrix with
349 read coverage. We QCed samples with log(total mapped fragments) fewer than mean – 2SD
350 across samples in each cell type. We QCed peaks so that at least two individuals have any
351 fragments for the peak. We then ran RASQUAL software with the inter-individual differences in
352 ATAC peak counts (in a peak by donor matrix) and intra-individual allelic imbalance (in VCF),
353 with accounting for chromatin accessibility PCs (the first *N* components whose explained
354 variances are greater than those from permutation result), 3 genotype PCs, sample site and sex
355 as covariates. RASQUAL output chi-squared statistics and *P* values. We computed FDR from
356 these raw *P* values by Benjamini & Hochberg correction on local multiple test burden (i.e., the
357 number of *cis*-SNPs in the region). To correct for genome-wide multiple testing, we ran the
358 RASQUAL with random permutation, where the relationship between sample labels and the
359 count matrix was broken. Thus, we derived *q* values for each candidate caQTL.

360 We finally intersected these peaks with significant caQTL effect in each significance
361 threshold with SCENT peaks and assessed causal variants enrichment within these peaks for
362 GWAS as explained in the previous sections.

363

364 *ClinVar analysis*

365 We downloaded the latest clinically reported variant list registered at ClinVar from
366 https://ftp.ncbi.nlm.nih.gov/pub/clinvar/vcf_GRCh38/clinvar.vcf.gz. We then screened the
367 variants to exclude (1) exonic variants and (2) variants categorized as “benign”. We defined the

368 ClinVar variant density as the number of the non-coding and non-benign variants within each
369 annotation x 1,000 divided by the total length (bp) of each annotation.
370
371 *Somatic mutation analysis*
372 We used a list of somatic mutation hotspot in Supplementary Table 2-20 of the original
373 publication[95]. We lifted the genomic coordinates to GRCh38 by using LifOver software. We then
374 intersected the non-coding somatic mutation hotspots with our cell-type-specific SCENT peaks.
375 We compared the intersected elements' target genes by SCENT with the "Annotate_Gene"
376 column from the original publication.
377
378 *Downsampling experiments*
379 To evaluate the effect of cell numbers on the statistical power in detecting significant SCENT
380 enhancer-gene linkages, we performed downsampling experiments in fibroblast (the most
381 abundant cell type in arthritis-tissue dataset, n_{cell} = 9,905). We randomly samples cells (n_{cell} =
382 500, 1000, 2500, 5000, and 7500). We then applied SCENT to each of the subset groups of
383 cells and defined significant peak-gene links with FDR < 10%. We counted the number of
384 significant peak-gene links in each of the subset groups of cells, and annotated peaks based on
385 the distance to the TSS to the target gene.
386
387 **References**
388 1. Welter, D., MacArthur, J., Morales, J., Burdett, T., Hall, P., Junkins, H., Klemm, A.,
389 Flicek, P., Manolio, T., Hindorff, L., et al. (2014). The NHGRI GWAS Catalog, a curated

390 resource of SNP-trait associations. Nucleic Acids Res *42*, D1001-6.
391 10.1093/nar/gkt1229.
392 2. Visscher, P.M., Wray, N.R., Zhang, Q., Sklar, P., McCarthy, M.I., Brown, M.A., and
393 Yang, J. (2017). 10 Years of GWAS Discovery: Biology, Function, and Translation. Am J
394 Hum Genet *101*, 5–22. 10.1016/J.AJHG.2017.06.005.
395 3. Buniello, A., Macarthur, J.A.L., Cerezo, M., Harris, L.W., Hayhurst, J., Malangone, C.,
396 McMahon, A., Morales, J., Mountjoy, E., Sollis, E., et al. (2019). The NHGRI-EBI GWAS
397 Catalog of published genome-wide association studies, targeted arrays and summary
398 statistics 2019. Nucleic Acids Res *47*, D1005–D1012. 10.1093/NAR/GKY1120.
399 4. Claussnitzer, M., Cho, J.H., Collins, R., Cox, N.J., Dermitzakis, E.T., Hurles, M.E.,
900 Kathiresan, S., Kenny, E.E., Lindgren, C.M., MacArthur, D.G., et al. (2020). A brief
901 history of human disease genetics. Nature 2020 577:7789 *577*, 179–189.
902 10.1038/s41586-019-1879-7.
903 5. Plenge, R.M., Scolnick, E.M., and Altshuler, D. (2013). Validating therapeutic targets
904 through human genetics. Nature Reviews Drug Discovery 2013 12:8 *12*, 581–594.
905 10.1038/nrd4051.
906 6. Shendure, J., Findlay, G.M., and Snyder, M.W. (2019). Genomic Medicine–Progress,
907 Pitfalls, and Promise. Cell *177*, 45–57. 10.1016/J.CELL.2019.02.003.
908 7. Schaid, D.J., Chen, W., and Larson, N.B. (2018). From genome-wide associations to
909 candidate causal variants by statistical fine-mapping. Nature Reviews Genetics 2018
910 19:8 *19*, 491–504. 10.1038/s41576-018-0016-z.
911 8. Maurano, M.T., Humbert, R., Rynes, E., Thurman, R.E., Haugen, E., Wang, H.,
912 Reynolds, A.P., Sandstrom, R., Qu, H., Brody, J., et al. (2012). Systematic localization of
913 common disease-associated variation in regulatory DNA. Science (1979) *337*, 1190–
914 1195. 10.1126/SCIENCE.1222794/SUPPL_FILE/MAURANO.SM.PDF.
915 9. Edwards, S.L., Beesley, J., French, J.D., and Dunning, M. (2013). Beyond GWASs:
916 illuminating the dark road from association to function. Am J Hum Genet *93*, 779–797.
917 10.1016/J.AJHG.2013.10.012.
918 10. Trynka, G., Sandor, C., Han, B., Xu, H., Stranger, B.E., Liu, X.S., and Raychaudhuri, S.
919 (2013). Chromatin marks identify critical cell types for fine mapping complex trait
920 variants. Nat Genet *45*, 124–130. 10.1038/ng.2504.

921 11. Sanyal, A., Lajoie, B.R., Jain, G., and Dekker, J. (2012). The long-range interaction
922 landscape of gene promoters. Nature 2012 489:7414 *489*, 109–113.
923 10.1038/nature11279.
924 12. Smemo, S., Tena, J.J., Kim, K.H., Gamazon, E.R., Sakabe, N.J., Gómez-Marín, C.,
925 Aneas, I., Credidio, F.L., Sobreira, D.R., Wasserman, N.F., et al. (2014). Obesity-
926 associated variants within FTO form long-range functional connections with IRX3. Nature
927 2014 507:7492 *507*, 371–375. 10.1038/nature13138.
928 13. Won, H., de La Torre-Ubieta, L., Stein, J.L., Parikshak, N.N., Huang, J., Opland, C.K.,
929 Gandal, M.J., Sutton, G.J., Hormozdiari, F., Lu, D., et al. (2016). Chromosome
930 conformation elucidates regulatory relationships in developing human brain. Nature 2016
931 538:7626 *538*, 523–527. 10.1038/nature19847.
932 14. Strober, B.J., Elorbany, R., Rhodes, K., Krishnan, N., Tayeb, K., Battle, A., and Gilad, Y.
933 (2019). Dynamic genetic regulation of gene expression during cellular differentiation.
934 Science *364*, 1287–1290. 10.1126/SCIENCE.AAW0040.
935 15. Cuomo, A.S.E., Seaton, D.D., McCarthy, D.J., Martinez, I., Bonder, M.J., Garcia-
936 Bernardo, J., Amatya, S., Madrigal, P., Isaacson, A., Buettner, F., et al. (2020). Single-
937 cell RNA-sequencing of differentiating iPS cells reveals dynamic genetic effects on gene
938 expression. Nature Communications 2020 11:1 *11*, 1–14. 10.1038/s41467-020-14457-z.
939 16. Zhernakova, D. v., Deelen, P., Vermaat, M., van Iterson, M., van Galen, M., Arindrarto,
940 W., Van't Hof, P., Mei, H., van Dijk, F., Westra, H.J., et al. (2017). Identification of
941 context-dependent expression quantitative trait loci in whole blood. Nat Genet *49*, 139–
942 145. 10.1038/NG.3737.
943 17. Nathan, A., Asgari, S., Ishigaki, K., Valencia, C., Amariuta, T., Luo, Y., Beynor, J.I.,
944 Baglaenko, Y., Suliman, S., Price, A.L., et al. (2022). Single-cell eQTL models reveal
945 dynamic T cell state dependence of disease loci. Nature 2022 606:7912 *606*, 120–128.
946 10.1038/s41586-022-04713-1.
947 18. Wakefield, J. (2007). A Bayesian Measure of the Probability of False Discovery in
948 Genetic Epidemiology Studies. Am J Hum Genet *81*, 208. 10.1086/519024.
949 19. Maller, J.B., McVean, G., Byrnes, J., Vukcevic, D., Palin, K., Su, Z., Howson, J.M.M.,
950 Auton, A., Myers, S., Morris, A., et al. (2012). Bayesian refinement of association signals
951 for 14 loci in 3 common diseases. Nat Genet *44*, 1294–1301. 10.1038/NG.2435.

952 20. Hormozdiari, F., Kostem, E., Kang, E.Y., Pasaniuc, B., and Eskin, E. (2014). Identifying
953 causal variants at loci with multiple signals of association. Genetics *198*, 497–508.
954 10.1534/GENETICS.114.167908.
955 21. Benner, C., Spencer, C.C.A., Havulinna, A.S., Salomaa, V., Ripatti, S., and Pirinen, M.
956 (2016). FINEMAP: efficient variable selection using summary data from genome-wide
957 association studies. Bioinformatics *32*, 1493–1501.
958 10.1093/BIOINFORMATICS/BTW018.
959 22. Wang, G., Sarkar, A., Carbonetto, P., and Stephens, M. (2020). A simple new approach
960 to variable selection in regression, with application to genetic fine mapping. J R Stat Soc
961 Series B Stat Methodol *82*, 1273–1300. 10.1111/RSSB.12388.
962 23. Weissbrod, O., Hormozdiari, F., Benner, C., Cui, R., Ulirsch, J., Gazal, S., Schoech,
963 A.P., van de Geijn, B., Reshef, Y., Márquez-Luna, C., et al. (2020). Functionally informed
964 fine-mapping and polygenic localization of complex trait heritability. Nature Genetics
965 2020 52:12 *52*, 1355–1363. 10.1038/s41588-020-00735-5.
966 24. Wojcik, G.L., Graff, M., Nishimura, K.K., Tao, R., Haessler, J., Gignoux, C.R., Highland,
967 H.M., Patel, Y.M., Sorokin, E.P., Avery, C.L., et al. (2019). Genetic analyses of diverse
968 populations improves discovery for complex traits. Nature 2019 570:7762 *570*, 514–518.
969 10.1038/s41586-019-1310-4.
970 25. Chen, M.H., Raffield, L.M., Mousas, A., Sakaue, S., Huffman, J.E., Moscati, A., Trivedi,
971 B., Jiang, T., Akbari, P., Vuckovic, D., et al. (2020). Trans-ethnic and Ancestry-Specific
972 Blood-Cell Genetics in 746,667 Individuals from 5 Global Populations. Cell *182*, 1198-
973 1213.e14. 10.1016/J.CELL.2020.06.045.
974 26. Ishigaki, K., Sakaue, S., Terao, C., Luo, Y., Sonehara, K., Yamaguchi, K., Amariuta, T.,
975 Too, C.L., Laufer, V.A., Scott, I.C., et al. (2021). Trans-ancestry genome-wide
976 association study identifies novel genetic mechanisms in rheumatoid arthritis. medRxiv
977 *12*, 2021.12.01.21267132. 10.1101/2021.12.01.21267132.
978 27. Kichaev, G., and Pasaniuc, B. (2015). Leveraging Functional-Annotation Data in Trans-
979 ethnic Fine-Mapping Studies. Am J Hum Genet *97*, 260–271.
980 10.1016/J.AJHG.2015.06.007.
981 28. Kanai, M., Ulirsch, J.C., Karjalainen, J., Kurki, M., Karczewski, K.J., Fauman, E., Wang,
982 Q.S., Jacobs, H., Aguet, F., Ardlie, K.G., et al. (2021). Insights from complex trait fine-

983 mapping across diverse populations. medRxiv, 2021.09.03.21262975.
984 10.1101/2021.09.03.21262975.
985 29. Huang, H., Fang, M., Jostins, L., Umićević Mirkov, M., Boucher, G., Anderson, C.A.,
986 Andersen, V., Cleynen, I., Cortes, A., Crins, F., et al. (2017). Fine-mapping inflammatory
987 bowel disease loci to single-variant resolution. Nature *547*, 173–178.
988 10.1038/NATURE22969.
989 30. Farh, K.K.H., Marson, A., Zhu, J., Kleinewietfeld, M., Housley, W.J., Beik, S., Shoresh,
990 N., Whitton, H., Ryan, R.J.H., Shishkin, A.A., et al. (2014). Genetic and epigenetic fine
991 mapping of causal autoimmune disease variants. Nature 2014 518:7539 *518*, 337–343.
992 10.1038/nature13835.
993 31. Mahajan, A., Taliun, D., Thurner, M., Robertson, N.R., Torres, J.M., Rayner, N.W.,
994 Payne, A.J., Steinthorsdottir, V., Scott, R.A., Grarup, N., et al. (2018). Fine-mapping type
995 2 diabetes loci to single-variant resolution using high-density imputation and islet-specific
996 epigenome maps. Nature Genetics 2018 50:11 *50*, 1505–1513. 10.1038/s41588-018-
997 0241-6.
998 32. Kichaev, G., Yang, W.Y., Lindstrom, S., Hormozdiari, F., Eskin, E., Price, A.L., Kraft, P.,
999 and Pasaniuc, B. (2014). Integrating functional data to prioritize causal variants in
1000 statistical fine-mapping studies. PLoS Genet *10*. 10.1371/JOURNAL.PGEN.1004722.
1001 33. Roadmap Epigenomics Consortium, Kundaje, A., Meuleman, W., Ernst, J., Bilenky, M.,
1002 Yen, A., Heravi-Moussavi, A., Kheradpour, P., Zhang, Z., Wang, J., et al. (2015).
1003 Integrative analysis of 111 reference human epigenomes. Nature 2015 518:7539 *518*,
1004 317–330. 10.1038/nature14248.
1005 34. Chen, L., Ge, B., Casale, F.P., Vasquez, L., Kwan, T., Garrido-Martín, D., Watt, S., Yan,
1006 Y., Kundu, K., Ecker, S., et al. (2016). Genetic Drivers of Epigenetic and Transcriptional
1007 Variation in Human Immune Cells. Cell *167*, 1398-1414.e24. 10.1016/j.cell.2016.10.026.
1008 35. Dunham, I., Kundaje, A., Aldred, S.F., Collins, P.J., Davis, C.A., Doyle, F., Epstein, C.B.,
1009 Frietze, S., Harrow, J., Kaul, R., et al. (2012). An integrated encyclopedia of DNA
1010 elements in the human genome. Nature *489*, 57–74. 10.1038/NATURE11247.
1011 36. Ernst, J., Kheradpour, P., Mikkelsen, T.S., Shoresh, N., Ward, L.D., Epstein, C.B.,
1012 Zhang, X., Wang, L., Issner, R., Coyne, M., et al. (2011). Mapping and analysis of
1013 chromatin state dynamics in nine human cell types. Nature 2011 473:7345 *473*, 43–49.
1014 10.1038/nature09906.

37. Boix, C.A., James, B.T., Park, Y.P., Meuleman, W., and Kellis, M. (2021). Regulatory genomic circuitry of human disease loci by integrative epigenomics. Nature 2021 590:7845 *590*, 300–307. 10.1038/s41586-020-03145-z.
38. Fulco, C.P., Nasser, J., Jones, T.R., Munson, G., Bergman, D.T., Subramanian, V., Grossman, S.R., Anyoha, R., Doughty, B.R., Patwardhan, T.A., et al. (2019). Activity-by-Contact model of enhancer-promoter regulation from thousands of CRISPR perturbations. Nat Genet *51*, 1664. 10.1038/S41588-019-0538-0.
39. Nasser, J., Bergman, D.T., Fulco, C.P., Guckelberger, P., Doughty, B.R., Patwardhan, T.A., Jones, T.R., Nguyen, T.H., Ulirsch, J.C., Lekschas, F., et al. (2021). Genome-wide enhancer maps link risk variants to disease genes. Nature 2021 593:7858 *593*, 238–243. 10.1038/s41586-021-03446-x.
40. Gazal, S., Weissbrod, O., Hormozdiari, F., Dey, K.K., Nasser, J., Jagadeesh, K.A., Weiner, D.J., Shi, H., Fulco, C.P., O'Connor, L.J., et al. (2022). Combining SNP-to-gene linking strategies to identify disease genes and assess disease omnigenicity. Nat Genet *54*, 827–836. 10.1038/S41588-022-01087-Y.
41. Pickar-Oliver, A., and Gersbach, C.A. (2019). The next generation of CRISPR–Cas technologies and applications. Nature Reviews Molecular Cell Biology 2019 20:8 *20*, 490–507. 10.1038/s41580-019-0131-5.
42. Anzalone, A. v., Koblan, L.W., and Liu, D.R. (2020). Genome editing with CRISPR–Cas nucleases, base editors, transposases and prime editors. Nature Biotechnology 2020 38:7 *38*, 824–844. 10.1038/s41587-020-0561-9.
43. Baglaenko, Y., Macfarlane, D., Marson, A., Nigrovic, P.A., and Raychaudhuri, S. (2021). Genome editing to define the function of risk loci and variants in rheumatic disease. Nature Reviews Rheumatology 2021 17:8 *17*, 462–474. 10.1038/s41584-021-00637-8.
44. Cao, J., Cusanovich, D.A., Ramani, V., Aghamirzaie, D., Pliner, H.A., Hill, A.J., Daza, R.M., McFaline-Figueroa, J.L., Packer, J.S., Christiansen, L., et al. (2018). Joint profiling of chromatin accessibility and gene expression in thousands of single cells. Science (1979) *361*, 1380–1385. 10.1126/SCIENCE.AAU0730/SUPPL_FILE/AAU0730_TABLESS1_S13.XLSX.
45. Chen, S., Lake, B.B., and Zhang, K. (2019). High-throughput sequencing of the transcriptome and chromatin accessibility in the same cell. Nature Biotechnology 2019 37:12 *37*, 1452–1457. 10.1038/s41587-019-0290-0.

46. Ma, S., Zhang, B., LaFave, L.M., Earl, A.S., Chiang, Z., Hu, Y., Ding, J., Brack, A., Kartha, V.K., Tay, T., et al. (2020). Chromatin Potential Identified by Shared Single-Cell Profiling of RNA and Chromatin. Cell *183*, 1103-1116.e20. 10.1016/J.CELL.2020.09.056.
47. Allaway, K.C., Gabitto, M.I., Wapinski, O., Saldi, G., Wang, C.Y., Bandler, R.C., Wu, S.J., Bonneau, R., and Fishell, G. (2021). Genetic and epigenetic coordination of cortical interneuron development. Nature 2021 597:7878 *597*, 693–697. 10.1038/s41586-021-03933-1.
48. Trevino, A.E., Müller, F., Andersen, J., Sundaram, L., Kathiria, A., Shcherbina, A., Farh, K., Chang, H.Y., Pașca, A.M., Kundaje, A., et al. (2021). Chromatin and gene-regulatory dynamics of the developing human cerebral cortex at single-cell resolution. Cell *184*, 5053-5069.e23. 10.1016/J.CELL.2021.07.039.
49. Granja, J.M., Corces, M.R., Pierce, S.E., Bagdatli, S.T., Choudhry, H., Chang, H.Y., and Greenleaf, W.J. (2021). ArchR is a scalable software package for integrative single-cell chromatin accessibility analysis. Nature Genetics 2021 53:3 *53*, 403–411. 10.1038/s41588-021-00790-6.
50. Stuart, T., Srivastava, A., Madad, S., Lareau, C.A., and Satija, R. (2021). Single-cell chromatin state analysis with Signac. Nature Methods 2021 18:11 *18*, 1333–1341. 10.1038/s41592-021-01282-5.
51. Pliner, H.A., Packer, J.S., McFaline-Figueroa, J.L., Cusanovich, D.A., Daza, R.M., Aghamirzaie, D., Srivatsan, S., Qiu, X., Jackson, D., Minkina, A., et al. (2018). Cicero Predicts cis-Regulatory DNA Interactions from Single-Cell Chromatin Accessibility Data. Mol Cell *71*, 858-871.e8. 10.1016/J.MOLCEL.2018.06.044.
52. Efron, B., and Tibshirani, R.J. (1994). An Introduction to the Bootstrap. An Introduction to the Bootstrap. 10.1201/9780429246593.
53. Lähnemann, D., Köster, J., Szczurek, E., McCarthy, D.J., Hicks, S.C., Robinson, M.D., Vallejos, C.A., Campbell, K.R., Beerenwinkel, N., Mahfouz, A., et al. (2020). Eleven grand challenges in single-cell data science. Genome Biology 2020 21:1 *21*, 1–35. 10.1186/S13059-020-1926-6.
54. Sarkar, A., and Stephens, M. (2021). Separating measurement and expression models clarifies confusion in single-cell RNA sequencing analysis. Nature Genetics 2021 53:6 *53*, 770–777. 10.1038/s41588-021-00873-4.

55. Chen, H., Lareau, C., Andreani, T., Vinyard, M.E., Garcia, S.P., Clement, K., Andrade-Navarro, M.A., Buenrostro, J.D., and Pinello, L. (2019). Assessment of computational methods for the analysis of single-cell ATAC-seq data. Genome Biol *20*, 1–25. 10.1186/S13059-019-1854-5/FIGURES/7.
56. Granja, J.M., Klemm, S., McGinnis, L.M., Kathiria, A.S., Mezger, A., Corces, M.R., Parks, B., Gars, E., Liedtke, M., Zheng, G.X.Y., et al. (2019). Single-cell multiomic analysis identifies regulatory programs in mixed-phenotype acute leukemia. Nature Biotechnology 2019 37:12 *37*, 1458–1465. 10.1038/s41587-019-0332-7.
57. Townes, F.W., Hicks, S.C., Aryee, M.J., and Irizarry, R.A. (2019). Feature selection and dimension reduction for single-cell RNA-Seq based on a multinomial model. Genome Biol *20*, 1–16. 10.1186/S13059-019-1861-6/FIGURES/5.
58. Luecken, M.D., Burkhardt, D.B., Cannoodt, R., Lance, C., Agrawal, A., Aliee, H., Chen, A.T., Deconinck, L., Detweiler, A.M., Granados, A., et al. (2021). A sandbox for prediction and integration of DNA, RNA, and proteins in single cells. Proceedings of the Neural Information Processing Systems Track on Datasets and Benchmarks *1*.
59. Mimitou, E.P., Lareau, C.A., Chen, K.Y., Zorzetto-Fernandes, A.L., Hao, Y., Takeshima, Y., Luo, W., Huang, T.S., Yeung, B.Z., Papalexi, E., et al. (2021). Scalable, multimodal profiling of chromatin accessibility, gene expression and protein levels in single cells. Nat Biotechnol *39*, 1246–1258. 10.1038/S41587-021-00927-2.
60. Chen, A.F., Parks, B., Kathiria, A.S., Ober-Reynolds, B., Goronzy, J.J., and Greenleaf, W.J. (2022). NEAT-seq: simultaneous profiling of intra-nuclear proteins, chromatin accessibility and gene expression in single cells. Nature Methods 2022 19:5 *19*, 547–553. 10.1038/s41592-022-01461-y.
61. Meijer, M., Agirre, E., Kabbe, M., van Tuijn, C.A., Heskol, A., Zheng, C., Mendanha Falcão, A., Bartosovic, M., Kirby, L., Calini, D., et al. (2022). Epigenomic priming of immune genes implicates oligodendroglia in multiple sclerosis susceptibility. Neuron *110*, 1193-1210.e13. 10.1016/J.NEURON.2021.12.034.
62. Zhang, Z., Zamojski, M., Smith, G.R., Willis, T.L., Yianni, V., Mendelev, N., Pincas, H., Seenarine, N., Amper, M.A.S., Vasoya, M., et al. (2022). Single nucleus transcriptome and chromatin accessibility of postmortem human pituitaries reveal diverse stem cell regulatory mechanisms. Cell Rep *38*. 10.1016/J.CELREP.2022.110467.

63. Abascal, F., Acosta, R., Addleman, N.J., Adrian, J., Afzal, V., Aken, B., Akiyama, J.A., Jammal, O. al, Amrhein, H., Anderson, S.M., et al. (2020). Expanded encyclopaedias of DNA elements in the human and mouse genomes. Nature 2020 583:7818 *583*, 699–710. 10.1038/s41586-020-2493-4.

64. Westra, H.J., and Franke, L. (2014). From genome to function by studying eQTLs. Biochim Biophys Acta *1842*, 1896–1902. 10.1016/J.BBADIS.2014.04.024.

65. Hujoel, M.L.A., Gazal, S., Hormozdiari, F., van de Geijn, B., and Price, A.L. (2019). Disease Heritability Enrichment of Regulatory Elements Is Concentrated in Elements with Ancient Sequence Age and Conserved Function across Species. Am J Hum Genet *104*, 611–624. 10.1016/j.ajhg.2019.02.008.

66. Siepel, A., Bejerano, G., Pedersen, J.S., Hinrichs, A.S., Hou, M., Rosenbloom, K., Clawson, H., Spieth, J., Hillier, L.D.W., Richards, S., et al. (2005). Evolutionarily conserved elements in vertebrate, insect, worm, and yeast genomes. Genome Res *15*, 1034–1050. 10.1101/GR.3715005.

67. Lek, M., Karczewski, K.J., Minikel, E. v., Samocha, K.E., Banks, E., Fennell, T., O'Donnell-Luria, A.H., Ware, J.S., Hill, A.J., Cummings, B.B., et al. (2016). Analysis of protein-coding genetic variation in 60,706 humans. Nature *536*, 285–291. 10.1038/nature19057.

68. Karczewski, K.J., Francioli, L.C., Tiao, G., Cummings, B.B., Alföldi, J., Wang, Q., Collins, R.L., Laricchia, K.M., Ganna, A., Birnbaum, D.P., et al. (2020). The mutational constraint spectrum quantified from variation in 141,456 humans. Nature *581*, 434–443. 10.1038/s41586-020-2308-7.

69. Wang, X., and Goldstein, D.B. (2020). Enhancer Domains Predict Gene Pathogenicity and Inform Gene Discovery in Complex Disease. The American Journal of Human Genetics *106*, 215–233. 10.1016/J.AJHG.2020.01.012.

70. Aguet, F., Barbeira, A.N., Bonazzola, R., Brown, A., Castel, S.E., Jo, B., Kasela, S., Kim-Hellmuth, S., Liang, Y., Oliva, M., et al. (2020). The GTEx Consortium atlas of genetic regulatory effects across human tissues. Science *369*, 1318. 10.1126/SCIENCE.AAZ1776.

71. Kurki, M.I., Karjalainen, J., Palta, P., Sipilä, T.P., Kristiansson, K., Donner, K., Reeve, M.P., Laivuori, H., Aavikko, M., Kaunisto, M.A., et al. (2022). FinnGen: Unique genetic

140 insights from combining isolated population and national health register data. medRxiv,
141 2022.03.03.22271360. 10.1101/2022.03.03.22271360.
142 72. Bycroft, C., Freeman, C., Petkova, D., Band, G., Elliott, L.T., Sharp, K., Motyer, A.,
143 Vukcevic, D., Delaneau, O., O'Connell, J., et al. (2018). The UK Biobank resource with
144 deep phenotyping and genomic data. Nature *562*, 203–209. 10.1038/s41586-018-0579-
145 z.
146 73. Dey, K.K., Gazal, S., van de Geijn, B., Kim, S.S., Nasser, J., Engreitz, J.M.,
147 Correspondence, A.L.P., and Price, A.L. (2022). SNP-to-gene linking strategies reveal
148 contributions of enhancer-related and candidate master-regulator genes to autoimmune
149 disease. Cell Genomics *2*, 100145. 10.1016/j.xgen.2022.100145.
150 74. Freund, M.K., Burch, K.S., Shi, H., Mancuso, N., Kichaev, G., Garske, K.M., Pan, D.Z.,
151 Miao, Z., Mohlke, K.L., Laakso, M., et al. (2018). Phenotype-Specific Enrichment of
152 Mendelian Disorder Genes near GWAS Regions across 62 Complex Traits. The
153 American Journal of Human Genetics *103*, 535–552. 10.1016/J.AJHG.2018.08.017.
154 75. Gate, R.E., Cheng, C.S., Aiden, A.P., Siba, A., Tabaka, M., Lituiev, D., Machol, I.,
155 Gordon, M.G., Subramaniam, M., Shamim, M., et al. (2018). Genetic determinants of co-
156 accessible chromatin regions in activated T cells across humans. Nature Genetics 2018
157 50:8 *50*, 1140–1150. 10.1038/s41588-018-0156-2.
158 76. Khetan, S., Kursawe, R., Youn, A., Lawlor, N., Jillette, A., Marquez, E.J., Ucar, D., and
159 Stitzel, M.L. (2018). Type 2 Diabetes-Associated Genetic Variants Regulate Chromatin
160 Accessibility in Human Islets. Diabetes *67*, 2466–2477. 10.2337/DB18-0393.
161 77. Alasoo, K., Rodrigues, J., Mukhopadhyay, S., Knights, A.J., Mann, A.L., Kundu, K., Hale,
162 C., Dougan, G., and Gaffney, D.J. (2018). Shared genetic effects on chromatin and gene
163 expression indicate a role for enhancer priming in immune response. Nat Genet *50*, 424.
164 10.1038/S41588-018-0046-7.
165 78. Currin, K.W., Erdos, M.R., Narisu, N., Rai, V., Vadlamudi, S., Perrin, H.J., Idol, J.R., Yan,
166 T., Albanus, R.D.O., Broadaway, K.A., et al. (2021). Genetic effects on liver chromatin
167 accessibility identify disease regulatory variants. Am J Hum Genet *108*, 1169–1189.
168 10.1016/J.AJHG.2021.05.001.
169 79. Kumasaka, N., Knights, A.J., and Gaffney, D.J. (2015). Fine-mapping cellular QTLs with
170 RASQUAL and ATAC-seq. Nature Genetics 2015 48:2 *48*, 206–213. 10.1038/ng.3467.

171 80. Chiou, J., Geusz, R.J., Okino, M.L., Han, J.Y., Miller, M., Melton, R., Beebe, E.,
172 Benaglio, P., Huang, S., Korgaonkar, K., et al. (2021). Interpreting type 1 diabetes risk
173 with genetics and single-cell epigenomics. Nature 2021 594:7863 *594*, 398–402.
174 10.1038/s41586-021-03552-w.
175 81. Mouri, K., Guo, M.H., de Boer, C.G., Lissner, M.M., Harten, I.A., Newby, G.A., DeBerg,
176 H.A., Platt, W.F., Gentili, M., Liu, D.R., et al. (2022). Prioritization of autoimmune
177 disease-associated genetic variants that perturb regulatory element activity in T cells.
178 Nature Genetics 2022 54:5 *54*, 603–612. 10.1038/s41588-022-01056-5.
179 82. Javierre, B.M., Sewitz, S., Cairns, J., Wingett, S.W., Várnai, C., Thiecke, M.J., Freire-
180 Pritchett, P., Spivakov, M., Fraser, P., Burren, O.S., et al. (2016). Lineage-Specific
181 Genome Architecture Links Enhancers and Non-coding Disease Variants to Target Gene
182 Promoters. Cell *167*, 1369-1384.e19. 10.1016/J.CELL.2016.09.037.
183 83. Radtke, F., Fasnacht, N., and MacDonald, H.R. (2010). Notch signaling in the immune
184 system. Immunity *32*, 14–27. 10.1016/J.IMMUNI.2010.01.004.
185 84. Wei, K., Korsunsky, I., Marshall, J.L., Gao, A., Watts, G.F.M., Major, T., Croft, A.P.,
186 Watts, J., Blazar, P.E., Lange, J.K., et al. (2020). Notch signalling drives synovial
187 fibroblast identity and arthritis pathology. Nature *582*, 259–264. 10.1038/S41586-020-
188 2222-Z.
189 85. Delacher, M., Schmidl, C., Herzig, Y., Breloer, M., Hartmann, W., Brunk, F., Kägebein,
190 D., Träger, U., Hofer, A.C., Bittner, S., et al. (2019). Rbpj expression in regulatory T cells
191 is critical for restraining TH2 responses. Nature Communications 2019 10:1 *10*, 1–20.
192 10.1038/s41467-019-09276-w.
193 86. Blake, J.A., Baldarelli, R., Kadin, J.A., Richardson, J.E., Smith, C.L., and Bult, C.J.
194 (2021). Mouse Genome Database (MGD): Knowledgebase for mouse–human
195 comparative biology. Nucleic Acids Res *49*, D981. 10.1093/NAR/GKAA1083.
196 87. Uhlén, M., Fagerberg, L., Hallström, B.M., Lindskog, C., Oksvold, P., Mardinoglu, A.,
197 Sivertsson, Å., Kampf, C., Sjöstedt, E., Asplund, A., et al. (2015). Tissue-based map of
198 the human proteome. Science (1979) *347*.
199 10.1126/SCIENCE.1260419/SUPPL_FILE/1260419_UHLEN.SM.PDF.
200 88. Hillier, S.G. (2001). Gonadotropic control of ovarian follicular growth and development.
201 Mol Cell Endocrinol *179*, 39–46. 10.1016/S0303-7207(01)00469-5.

202 89. Rubinstein, W.S., Maglott, D.R., Lee, J.M., Kattman, B.L., Malheiro, A.J., Ovetsky, M.,
203 Hem, V., Gorelenkov, V., Song, G., Wallin, C., et al. (2013). The NIH genetic testing
204 registry: a new, centralized database of genetic tests to enable access to comprehensive
205 information and improve transparency. Nucleic Acids Res *41*, D925–D935.
206 10.1093/NAR/GKS1173.
207 90. Retterer, K., Juusola, J., Cho, M.T., Vitazka, P., Millan, F., Gibellini, F., Vertino-Bell, A.,
208 Smaoui, N., Neidich, J., Monaghan, K.G., et al. (2016). Clinical application of whole-
209 exome sequencing across clinical indications. Genet Med *18*, 696–704.
210 10.1038/GIM.2015.148.
211 91. Adams, D.R., and Eng, C.M. (2018). Next-Generation Sequencing to Diagnose
212 Suspected Genetic Disorders. N Engl J Med *379*, 1353–1362.
213 10.1056/NEJMRA1711801.
214 92. Srivastava, S., Love-Nichols, J.A., Dies, K.A., Ledbetter, D.H., Martin, C.L., Chung,
215 W.K., Firth, H. v., Frazier, T., Hansen, R.L., Prock, L., et al. (2019). Meta-analysis and
216 multidisciplinary consensus statement: exome sequencing is a first-tier clinical diagnostic
217 test for individuals with neurodevelopmental disorders. Genet Med *21*, 2413–2421.
218 10.1038/S41436-019-0554-6.
219 93. Landrum, M.J., Lee, J.M., Benson, M., Brown, G.R., Chao, C., Chitipiralla, S., Gu, B.,
220 Hart, J., Hoffman, D., Jang, W., et al. (2018). ClinVar: improving access to variant
221 interpretations and supporting evidence. Nucleic Acids Res *46*, D1062–D1067.
222 10.1093/NAR/GKX1153.
223 94. Glocker, E.-O., Kotlarz, D., Boztug, K., Gertz, E.M., Schäffer, A.A., Noyan, F., Perro, M.,
224 Diestelhorst, J., Allroth, A., Murugan, D., et al. (2009). Inflammatory Bowel Disease and
225 Mutations Affecting the Interleukin-10 Receptor. New England Journal of Medicine *361*,
226 2033–2045.
227 10.1056/NEJMOA0907206/SUPPL_FILE/NEJM_GLOCKER_2033SA1.PDF.
228 95. Dietlein, F., Wang, A.B., Fagre, C., Tang, A., Besselink, N.J.M., Cuppen, E., Li, C.,
229 Sunyaev, S.R., Neal, J.T., and van Allen, E.M. (2022). Genome-wide analysis of somatic
230 noncoding mutation patterns in cancer. Science (1979) *376*.
231 10.1126/SCIENCE.ABG5601/SUPPL_FILE/SCIENCE.ABG5601_MDAR_REPRODUCIB
232 ILITY_CHECKLIST.PDF.

96. Connally, N., Nazeen, S., Lee, D., Shi, H., Stamatoyannopoulos, J., Chun, S., Cotsapas, C., Cassa, C.A., and Sunyaev, S. (2022). The missing link between genetic association and regulatory function. medRxiv, 2021.06.08.21258515. 10.1101/2021.06.08.21258515.
97. Donlin, L.T., Rao, D.A., Wei, K., Slowikowski, K., McGeachy, M.J., Turner, J.D., Meednu, N., Mizoguchi, F., Gutierrez-Arcelus, M., Lieb, D.J., et al. (2018). Methods for high-dimensonal analysis of cells dissociated from cyropreserved synovial tissue. Arthritis Res Ther *20*, 1–15. 10.1186/S13075-018-1631-Y/FIGURES/6.
98. Stuart, T., Butler, A., Hoffman, P., Hafemeister, C., Papalexi, E., Mauck, W.M., Hao, Y., Stoeckius, M., Smibert, P., and Satija, R. (2019). Comprehensive Integration of Single-Cell Data. Cell *177*, 1888-1902.e21. 10.1016/J.CELL.2019.05.031.
99. Korsunsky, I., Millard, N., Fan, J., Slowikowski, K., Zhang, F., Wei, K., Baglaenko, Y., Brenner, M., Loh, P. ru, and Raychaudhuri, S. (2019). Fast, sensitive and accurate integration of single-cell data with Harmony. Nature Methods 2019 16:12 *16*, 1289–1296. 10.1038/s41592-019-0619-0.
100. Delaneau, O., Marchini, J., and Zagury, J.F. (2012). A linear complexity phasing method for thousands of genomes. Nat Methods *9*, 179–181. 10.1038/nmeth.1785.
101. Das, S., Forer, L., Schönherr, S., Sidore, C., Locke, A.E., Kwong, A., Vrieze, S.I., Chew, E.Y., Levy, S., McGue, M., et al. (2016). Next-generation genotype imputation service and methods. Nature Genetics 2016 48:10 *48*, 1284–1287. 10.1038/ng.3656.
102. Gibbs, R.A., Boerwinkle, E., Doddapaneni, H., Han, Y., Korchina, V., Kovar, C., Lee, S., Muzny, D., Reid, J.G., Zhu, Y., et al. (2015). A global reference for human genetic variation. Nature *526*, 68–74. 10.1038/nature15393.
103. van de Geijn, B., Mcvicker, G., Gilad, Y., and Pritchard, J.K. (2015). WASP: allele-specific software for robust molecular quantitative trait locus discovery. Nat Methods *12*, 1061–1063. 10.1038/NMETH.3582.
104. van der Auwera, G., O'Connor, B., and Safari, an O.M.Company. (2020). Genomics in the Cloud.

Acknowledgments

We would like to sincerely thank participants of this study who provided tissue samples. We thank Anika Gupta, Joyce Kang and Kaitlyn Lagattuta for their comments and helpful discussion on the manuscript. This work is supported in part by funding from the National Institutes of Health (R01AR063759, U01HG012009, UC2AR081023). S.S. was in part supported by the Uehara Memorial Foundation and The Osamu Hayaishi Memorial Scholarship. K.Wei is supported by a Burroughs Wellcome Fund Career Awards for Medical Scientists, a Doris Duke Charitable Foundation Clinical Scientist Development Award, and a Rheumatology Research Foundation Innovative Research Award. We would like to thank the Brigham and Women's Hospital Center for Cellular Profiling Single Cell Mulitomics Core for experimental design and protocol optimization.

Author Contributions

S.S. and S.R. conceived the work and wrote the manuscript with critical input from co-authors. S.S. and K. Weinand analyzed the arthritis-tissue dataset and S.S. analyzed publicly available datasets with help and guidance from K.K.D., K.J., M.K., A.M., A.L.P., and S.R. G.F.M.W., Z.Z., M.B.B., L.T.D., and K.Wei provided samples and generated the arthritis-tissue dataset. S.I. refactored the SCENT software implementation as an R package.

Competing Financial Interests

We declare no conflict of interest for this study. S.R. is a founder for Mestag, Inc, a scientific advisor for Rheos, Jannsen, and Pfizer, and serves as a consultant for Sanofi and Abbvie.